The Astrophysical Journal, 889:162 (15pp), 2020 February 1 https://doi.org/10.3847/1538-4357/ab65fa

Probing the Full CO Spectral Line Energy Distribution (SLED) in the Nuclear Region of a Quasar-starburst System at $z = 6.003$

Jianan Li[1,2], Ran Wang[2,17], Dominik Riechers[3,4], Fabian Walter[4], Roberto Decarli[5], Bram P. Venamans[4], Roberto Neri[6], Yali Shao[1,2], Xiaohui Fan[7], Yu Gao[8,15], Chris L. Carilli[9,10], Alain Omont[11], Pierre Cox[11], Karl M. Menten[12], Jeff Wagg[13], Frank Bertoldi[14], and Desika Narayanan[16]

[1] Department of Astronomy, School of Physics, Peking University, Beijing 100871, People's Republic of China; jiananl@pku.edu.cn
[2] Kavli Institute for Astronomy and Astrophysics, Peking University, Beijing 100871, People's Republic of China; rwangkiaa@pku.edu.cn
[3] Department of Astronomy, Cornell University, Space Sciences Building, Ithaca, NY 14853, USA
[4] Max-Planck-Institut for Astronomie, Königstuhl 17, D-69117 Heidelberg, Germany
[5] INAF—Osservatorio di Astrofisica e Scienza dello Spazio, via Gobetti 93/3, I-40129 Bologna, Italy
[6] Institute de Radioastronomie Millimetrique, St. Martin d'Heres, F-38406, France
[7] Steward Observatory, University of Arizona, 933 North Cherry Avenue, Tucson, AZ 85721, USA
[8] Purple Mountain Observatory & Key Laboratory for Radio Astronomy, Chinese Academy of Sciences, 10 Yuanhua Road, Nanjing 210033, People's Republic of China
[9] Cavendish Laboratory, 19 J. J. Thomson Avenue, Cambridge CB3 0HE, UK
[10] National Radio Astronomy Observatory, Socorro, NM 87801-0387, USA
[11] Institut d'Astrophysique de Paris, Sorbonne Université, CNRS, UMR 7095, 98 bis bd Arago, F-75014 Paris, France
[12] Max-Planck-Institut für Radioastronomie, Auf dem Hügel 69, D-53121 Bonn, Germany
[13] SKA Organization, Lower Withington Macclesfield, Cheshire SK11 9DL, UK
[14] Argelander-Institut für Astronomie, University at Bonn, Auf dem Hügel 71, D-53121 Bonn, Germany
[15] Department of Astronomy, Xiamen University, Xiamen, Fujian 361005, China
[16] Department of Astronomy, University of Florida, 211 Bryant Space Science Center, Gainesville, FL 32611, USA
Received 2019 November 13; revised 2019 December 18; accepted 2019 December 27; published 2020 February 4

Abstract

We report Atacama Large Millimeter/submillimeter Array observations of CO(8–7), (9–8), $H_2O(2_{0,2}–1_{1,1})$, and $OH^+(1_1–0_1)$ and NOrthern Extended Millimeter Array observations of CO(5–4), (6–5), (12–11), and (13–12) toward the $z = 6.003$ quasar SDSS J231038.88+185519.7, aiming to probe the physical conditions of the molecular gas content of this source. We present the best sampled CO spectral line energy distribution (SLED) at $z = 6.003$, and analyzed it with the radiative transfer code MOLPOP-CEP. Fitting the CO SLED to a one-component model indicates a kinetic temperature $T_{\rm kin} = 228$ K, molecular gas density $\log(n(\rm H_2)/cm^{-3}) = 4.75$, and CO column density $\log(N(\rm CO)/cm^{-2}) = 17.5$; although, a two-component model better fits the data. In either case, the CO SLED is dominated by a "warm" and "dense" component. Compared to samples of local (Ultra) Luminous Infrared Galaxies, starburst galaxies, and high-redshift submillimeter galaxies, J2310+1855 exhibits higher CO excitation at ($J \geqslant 8$), like other high-redshift quasars. The high CO excitation, together with the enhanced $L_{\rm H_2O}/L_{\rm IR}$, $L_{\rm H_2O}/L_{\rm CO}$, and $L_{\rm OH^+}/L_{\rm H_2O}$ ratios, suggests that besides the UV radiation from young massive stars, other mechanisms such as shocks, cosmic-rays, and X-rays might also be responsible for the heating and ionization of the molecular gas. In the nuclear region probed by the molecular emissions lines, any of these mechanisms might be present due to the powerful quasar and the starburst activity.

Unified Astronomy Thesaurus concepts: Submillimeter astronomy (1647); Quasars (1319); Starburst galaxies (1570); Infrared galaxies (790); AGN host galaxies (2017); High-redshift galaxies (734); Interstellar medium (847); Molecular gas (1073); Interstellar phases (850); Early universe (435)

1. Introduction

The quasars discovered at $z \gtrsim 6$ represent the first generation of super massive black holes (SMBHs) and host galaxies. Many among these earliest systems host SMBHs of $\sim 10^9 M_\odot$ (e.g., Jiang et al. 2007, 2016), and the strong dust continuum and [C II] detections reveal dynamical masses of $\sim 10^{10}$–$10^{11} M_\odot$ and star formation rate (SFR) of $\sim 10^2$–$10^3 M_\odot$ yr^{-1} in the host galaxies (e.g., Maiolino et al. 2005; Wang et al. 2008, 2016, 2019b; Walter et al. 2009; Carilli & Walter 2013; Venemans et al. 2017b, 2019; Decarli et al. 2018; Neeleman et al. 2019). These suggest that the SMBH and galaxy coevolution is already in place in these $z \sim 6$ quasar-starburst systems. In the meantime, bright molecular CO emission lines are widely detected in starburst quasar hosts, which reveal a molecular gas content of $\sim 10^9$–$10^{10} M_\odot$ within a few kpc scale (e.g., Bertoldi et al. 2003; Walter et al. 2003; Riechers et al. 2009; Wang et al. 2010, 2011a, 2013, 2016; Carilli & Walter 2013; Venemans et al. 2017a). In particular, $z \gtrsim 6$ quasars are detected in very high (rotational quantum number) J (e.g., $J \geqslant 9$) CO transitions, indicating high CO excitation comparable to that found in local extreme (Ultra)luminous Infrared Galaxies ((U)LIRGs) and active galactic nuclei (AGNs; e.g., Gallerani et al. 2014; Wang et al. 2019a; Yang et al. 2019). Taking advantage of the most powerful sub/millimeter and radio facilities, such as Atacama Large Millimeter/submillimeter Array (ALMA), NOrthern Extended Millimeter Array (NOEMA), and the Karl G. Jansky Very Large Array (VLA), extensive observations at sub-mm/mm wavelengths have recently been carried out to search for the emission lines from the ionized, atomic, and molecular interstellar medium (ISM; e.g., Decarli et al. 2018; Hashimoto et al. 2018; Walter et al. 2018; Novak et al. 2019). These observations are crucial for our understanding of the physical,

[17] Corresponding author.

chemical conditions and kinematics of the multiphase ISM in these young quasar hosts at the earliest epoch and allow us to study the coevolution of SMBHs and their host galaxies at the earliest evolutionary phase.

CO emission lines have long been the workhorse probing molecular gas at rest-frame sub-mm band in the local and high-redshift universe. Low J (e.g., $J \lesssim 3$) CO emission lines are easy to excite in typical molecular cloud conditions (i.e., the lowest CO transition requires only ∼5 K above ground and densities of $\sim 100\,\mathrm{cm}^{-3}$); thus, it traces the bulk of the molecular gas content. Mid J (e.g., $4 \lesssim J \lesssim 8$) CO transitions are found to be linearly correlated with the far-infrared luminosity and trace the SFR (e.g., Greve et al. 2014; Liu et al. 2015). UV photons from newly formed high-mass stars are responsible for the molecular gas heating at this regime. The excitation of high J (e.g., $J \gtrsim 9$) CO transitions require both high temperature and high density, which are usually related to processes such as shocks, X-rays from AGNs, and cosmic-rays (Bradford et al. 2003; Spinoglio et al. 2012; Meijerink et al. 2013; Gallerani et al. 2014).

CO spectral line energy distribution (SLED)—the CO flux as a function of rotational quantum number J is a probe of the molecular gas physical conditions (e.g., temperature, density and illuminating radiation field strength). It has been used to study the physical conditions in a variety of local and high-redshift systems (e.g., Weiß et al. 2005, 2007; Riechers et al. 2006; Bradford et al. 2009, 2011; Spinoglio et al. 2012; Gallerani et al. 2014; Wang et al. 2019a; Yang et al. 2019). Normal star-forming galaxies have CO SLEDs that peak at relatively low J CO transitions. The CO SLED of the Milky Way's inner disk peaks at around $J = 3$–4 (Fixsen et al. 1999), and similar CO SLEDs are found in other local star-forming galaxies (Daddi et al. 2015). Galaxies that experience higher star formation activity than normal galaxies, e.g., starburst galaxies, (U)LIRGs, and submillimeter galaxies (SMGs), have moderately excited CO SLEDs that peak at higher J compared to the star-forming galaxies. One of the closest examples is the local starburst galaxy M82, whose CO SLED peaks at $J = 5$ in the central region and shows little line intensity at $J > 9$ (Weiß et al. 2005; Panuzzo et al. 2010). The molecular CO in luminous AGNs is usually highly excited. Very high J CO transitions ($J \gtrsim 9$) are detected in well-known AGNs such as NGC 1068 (Spinoglio et al. 2012), Mrk 231 (van der Werf et al. 2010), the Cloverleaf quasar at $z = 2.56$ (Bradford et al. 2009; Uzgil et al. 2016), and the $z = 3.9$ lensed quasar APM 08279+5255 (Weiß et al. 2007; Riechers et al. 2009; Bradford et al. 2011). And known to date, bright CO emission lines at $J \geqslant 10$ were detected in the host galaxies of three $z \geqslant 6$ quasars, i.e., SDSS J114816.64+525150.3 (hereafter J1148+5251) at $z = 6.4$ (e.g., Riechers et al. 2009; Gallerani et al. 2014), SDSS J010013.02+280225.8 (hereafter J0100+2802) at $z = 6.3$ (Wang et al. 2019a), and UHS J043947.08+163415.7 (hereafter J0439+1634) at $z = 6.5$ (Yang et al. 2019). The CO lines at $J \geqslant 10$ likely arose from warm gas with a kinetic temperature of $T_{\mathrm{kin}} \geqslant 100$ K. Kinetic temperature is proportional to kinetic energy through $T_{\mathrm{kin}} = \frac{2}{3}\frac{E_n}{k_b}$, where k_{B} is Boltzmann constant and E_n is the kinetic energy of the molecule. In the high-redshift quasars, X-rays from AGNs are frequently proposed to explain CO excitation at high J transitions (Bradford et al. 2009; Gallerani et al. 2014; Uzgil et al. 2016).

The H_2O and OH^+ lines provide additional diagnostics of heating and ionization sources of the molecular gas (e.g., Cosmic-rays, UV radiation, X-rays, and shocks) in addition to CO. The H_2O molecule traces the warm and dense molecular regions. It is found to be bright in infrared luminous galaxies and can even reach luminosities comparable to CO in these galaxies (van der Werf et al. 2011; Omont et al. 2013; Yang et al. 2013, 2016; Jarugula et al. 2019). Recent studies found a nearly linear relation between the water luminosity and the infrared luminosity in local and high-redshift systems over three orders of magnitude (González-Alfonso et al. 2010, 2014; Omont et al. 2013; Riechers et al. 2013; Yang et al. 2013, 2017; Jarugula et al. 2019). The brightest water lines are detected in the presence of shocks or X-rays (González-Alfonso et al. 2010; Pellegrini et al. 2013). Accordingly, the H_2O emission may even act as a tracer of the powering source of molecular gas, e.g., if the molecular gas is heated by the UV radiation or other mechanisms like shocks and X-rays. In addition, a variety of chemical processes are enrolled in the formation of H_2O and OH^+. The gas-phase H_2O molecule is formed by either solid-phase or gas-phase chemical reactions (Pellegrini et al. 2013; Yang et al. 2016). Neutral–neutral and ion–neutral reactions are two mechanisms to form H_2O molecules in the gas phase. The former is usually related to the shocks, while the latter is associated with PDRs, cosmic-ray-dominated regions, and X-ray-dominated regions (Yang et al. 2016). The molecular ions (e.g., H_2O^+, OH^+) as intermediates of the ion–neutral reactions, play important roles in distinguishing between shocks and PDR/XDR/cosmic-ray-dominated region. The bright H_2O^+ line detection in a sample of high-redshift lensed SMGs, for example, is probably initiated by cosmic-rays (Yang et al. 2016).

The OH^+ line, although not as strong as the turbulent gas tracer CH^+ that has been detected in high-redshift systems (e.g., Falgarone et al. 2017), traces the turbulent gas components as well, e.g., inflow or outflows. The formation of OH^+ requires both atomic and molecular hydrogen, at which column density the cosmic-rays or X-rays are more capable of penetrating and ionizing the neutral and molecular gas (e.g., van der Werf et al. 2010; Meijerink et al. 2011; González-Alfonso et al. 2018). The OH^+ line has been detected both in absorption (that probes the cold turbulent gas) and in emission, where the chemical structure is dominated by cosmic-ray ionization or X-ray radiation from AGNs (e.g., van der Werf et al. 2010; González-Alfonso et al. 2018). Limited by the weak strength and the P Cygni line profile (presence of both absorption and emission in the profile of the same spectral line), there is only one reported OH^+ line detection at $z \geqslant 6$ in absorption in the starburst galaxy HFLS3 (Riechers et al. 2013).

In order to understand the physical conditions and the heating mechanisms of the ISM in the complex environment with both AGN and nuclear starburst activities in these young quasar hosts at $z \sim 6$, we here present a study of the CO SLED in one of the most far-infrared and CO luminous quasars at $z \sim 6$, SDSS J231038.88+185519.7 (hereafter J2310+1855) at $z = 6.003$. J2310+1855 hosts a SMBH of $\approx 4 \times 10^9 M_\odot$ (Jiang et al. 2016). It was detected in bright dust continuum, CO(2–1) and (6–5), [C II] 158 μm, and [O III] 88 μm lines (Wang et al. 2013; Feruglio et al. 2018; Hashimoto et al. 2018; Odorico et al. 2018; Carniani et al. 2019; Shao et al. 2019). This quasar is also detected in bright CO(10–9) emission with a line flux of 1.04 ± 0.17 Jy km s^{-1} (D. A. Riechers et al. 2020, in preparation). The far-infrared dust emissions suggest the host galaxy is actively forming stars with an SFR of $\approx 2400\ M_\odot\ \mathrm{yr}^{-1}$ and is abundant in dust with a dust mass of $\approx 1.7 \times 10^9 M_\odot$ (Wang et al. 2013; Hashimoto et al. 2018; Carniani et al. 2019;

Shao et al. 2019). Wang et al. (2013), for the first time, spatially resolved the large amount of gas ($\approx 9.6 \times 10^{10}\,M_{\odot}$) residing in a $0\farcs55 \times 0\farcs40$ ($\sim$3 kpc) disk based on the [C II] 158 μm observations. The CO(2–1) emission line has a size comparable to the [C II] 158 μm emission with an associated molecular gas mass of $\approx 4.3 \times 10^{10}\,M_{\odot}$ (Shao et al. 2017). The [O III] 88 μm emission indicates an $L[\mathrm{O\ III}]/L_{\mathrm{IR}}$ ratio comparable to local systems at similar L_{IR}. The quasar is luminous in X-ray as well and has a derived $L_{2-10\,\mathrm{kev}} = 6.93 \times 10^{44}$ erg s^{-1} (Vito et al. 2019). In addition, there is evidence of companions close to the quasar although further confirmation is needed (Feruglio et al. 2018; Odorico et al. 2018). All together, J2310+1855 is an extraordinary quasar-starburst sample enabling us to study in detail an SMBH and galaxy coevolution at $z \sim 6$.

In this paper, we present our new ALMA observations of CO(8–7), (9–8), $H_2O(2_{0,2}–1_{1,1})$ and $OH^+(1_1–0_1)$ and NOEMA observation of CO(5–4), (6–5), (12–11), and (13–12) toward J2310+1855, aiming to investigate the molecular gas excitation mechanisms in environments of both intense star formation activity and luminous AGNs. The paper is organized as follows: In Sections 2 and 3, we present the observations and results. In Section 4, we analyze the CO SLED with a radiative transfer code to probe the physical conditions of molecular gas. In Section 5, we compare the CO excitation in J2310+1855 with local and high-redshift galaxy samples and AGNs and discuss the heating mechanisms of molecular gas as well. Finally, we summarize the results in Section 6. We adopt a flat ΛCDM cosmology with $H_0 = 70$ km s^{-1} Mpc^{-1} and $\Omega_{\mathrm{m}} = 0.3$, where $1''$ corresponds to 5.7 kpc at the J2310+1855 redshift ($z = 6.0031$), and the luminosity distance to J2310+1855 is 57763 Mpc.

2. Observations

2.1. ALMA

We observed the CO(8–7) ($\nu_{\mathrm{rest}} = 921.7997$ GHz), CO(9–8) ($\nu_{\mathrm{rest}} = 1036.9124$ GHz), $H_2O(2_{0,2}–1_{1,1})$ ($\nu_{\mathrm{rest}} = 987.9268$ GHz, hereafter H_2O) and $OH^+(1_1–0_1)$ ($\nu_{\mathrm{rest}} = 1033$ GHz, hereafter OH^+) emission lines, as well as the underlying continuum toward $z = 6.003$ quasar J2310+1855 with ALMA (Cycle 3, ID 2015.1.01265.S). All of the observations were executed between April and November in 2016 with beam sizes between $0\farcs6$ and $0\farcs8$. The CO(8–7), (9–8), H_2O, and OH^+ lines were observed in ALMA Band 4 with two separate executions, where 36 to 44 12 m diameter antennas were used during observations. For each observation, we used four spectral windows, each with a width of 1.875 GHz consisting of 128 channels, with two of the windows in the lower sideband (LSB) and the other two in the upper sideband (USB). The CO(8–7) and H_2O lines were observed in one spectral setup, with one spectral window centered on the CO(8–7) observed frequency of 131.6274 GHz, one window covering the H_2O emission, and the other two covering line-free dust continuum. In the other turning, we observed the CO(9–8) line centered at the frequency of 148.0648 GHz with the OH^+ line also covered in the same spectral window, while the other three windows measured the dust continuum. The fluxes were calibrated using the standard flux calibrator *Pallas*, while SDSS J2253+1608 was used as both the phase calibrator and the bandpass calibrator. The typical calibration uncertainty is <5% in ALMA band 4; here, we use 15% uncertainty that also includes the uncertainties of the old *Pallas* flux model in early casa versions (Stanley et al. 2019).

The observational data were calibrated and reduced with the Common Astronomy Software Applications (CASA) software package version 4.7.0 (McMullin et al. 2007), using the standard ALMA pipeline. The maps were generated using the CLEAN task in CASA, and we apply the robust weighting algorithm with a Briggs parameter of 2 equivalent to natural weighting. This results in an FWHM synthesized beam size of $0\farcs79 \times 0\farcs75$ and $0\farcs77 \times 0\farcs63$ at CO(8–7)(H_2O) and CO(9–8)(OH^+) observing frequency, and $0\farcs75 \times 0\farcs72$ and $0\farcs80 \times 0\farcs65$ at 136.6 and 141.1 GHz for the continuum. The continuum level was determined using a first-order polynomial, and the emission lines were imaged from the continuum subtracted data cube with all of the line-emitting channels included. With a total on-source time of 34.9 and 30.3 minutes for CO(8–7)(H_2O) and CO(9–8)(OH^+), we finally binned the data of CO(8–7)(H_2O) and CO(9–8)(OH^+) to 36 and 32 km s^{-1}, and the corresponding rms sensitivities were 0.17 and 0.19 mJy beam^{-1}, respectively. The sensitivity of the underlying continuum was 15 μJy beam^{-1}.

2.2. NOEMA

We observed CO(5–4) ($\nu_{\mathrm{rest}} = 576.2679$ GHz), CO(6–5) ($\nu_{\mathrm{rest}} = 691.4731$ GHz), CO(12–11) ($\nu_{\mathrm{rest}} = 1381.9951$ GHz), CO(13–12) ($\nu_{\mathrm{rest}} = 1496.9229$ GHz), and the underlying continuum of this quasar with NOEMA (Project W18EE). The CO(5–4) and (6–5) lines were observed in one tuning with the PolyFix correlator in Band 1 (3 mm), with the CO(5–4) line in the LSB and CO(6–5) in the USB, each with 7.744 GHz bandwidth. The observations were executed in the A configuration on 2019 January 18 with a total observing time of 2 hr, with 1.18 hr on source, while the rest of the time was expended for calibrations. A total of eight or nine antennas was used. The CO(12–11) and (13–12) lines were observed in the C/D configuration in Band 3 (1 mm) with one frequency setup, with the CO(12–11) line in the LSB and CO(13–12) in the USB, each with a 7.744 GHz bandwidth. The observations started on 2019 April 17 and ended on 2019 May 1. The total observing time was 8 hr with 6.2 hr on source, and a total number of 8–10 antennas were used in the observations. 3C454.3 was used as a phase calibrator throughout the entire CO observation. The typical calibration uncertainty is <10% in the 3 mm band and <20% in the 1 mm band.

The data were reduced with the Grenoble Image and Line Data Analysis System software (GILDAS; Guilloteau & Lucas 2000) packages CLIC and MAPPING. We extracted the continuum from all line free channels in the *uv* plane with UV_AVERAGE. The *uv* table of spectral lines was generated through UV_SUBTRACT with the underlying continuum subtracted. Both the *uv* table of the continuum and spectral lines were cleaned with the HOGBOM algorithm, and NATURAL weighting was used to ensure the maximum signal-to-noise ratio (S/N). This results in an FWHM synthesized beam size of $1\farcs67 \times 1\farcs37/1\farcs42 \times 1\farcs19$ for CO(5–4)/(6–5) and $2\farcs08 \times 1\farcs62/1\farcs91 \times 1\farcs53$ for CO(12–11)/(13–12). The calibrated data of CO(5–4) and (6–5) were smoothed by a factor of eight in frequency, resulting in a spectral resolution of 16 MHz ($\sim$60 km s^{-1}), and the calibrated CO(12–11) and (13–12) data were binned to 40 MHz ($\sim$60 km s^{-1}) resolution. The sensitivity was 0.32 mJy beam^{-1} for CO(5–4) and (6–5) and 0.54 mJy beam^{-1} for CO(12–11) and (13–12) per binned channels.

The observational details are listed in Table 1.

Table 1
Observational Details

Line ID	ν_{obs} (GHz)	$\delta\nu(\delta v)$ MHz (km s^{-1})	Band	T_{source} (min)	T_{tot} (min)	rms (mJy beam^{-1})
(1)	(2)	(3)	(4)	(5)	(6)	(7)
CO(5–4)	82.2875	16(58)	NOEMA 3 mm	70.8	120	0.32
CO(6–5)	98.7381	16(49)	…	…	…	…
CO(8–7)	131.6274	15.625(36)	ALMA Band 4	34.9	53.3	0.17
$H_2O(2_{0,2}–1_{1,1})$	141.0699	15.625(36)	…	…	…	…
CO(9–8)	148.0648	15.625(32)	ALMA Band 4	30.3	48.5	0.19
$OH^+(1_1–0_1)$	147.5061	15.625(32)	…	…	…	…
CO(12–11)	197.3405	40(61)	NOEMA 1 mm	372	600	0.54
CO(13–12)	213.7515	40(56)	…	…	…	…

Note. Column 1: Line ID; Column 2: Line center frequency in the observer frame; Column 3: Binned spectral resolution in frequency (velocity); Columns 4–7: Observing band, on-source time, total observing time, and achieved sensitivity per binned channel. The lines without on-source time are observed in the same frequency setup as the upper ones with on-source time listed in the table.

3. Results

With ALMA, we detect the CO(8–7), (9–8), and H_2O emission lines at 25σ, 22σ, and 15σ, respectively. The CO emission lines and the H_2O line are marginally resolved. We also obtained a tentative signal (4σ) for the OH^+ line close to the CO(9–8) line. The line intensity maps integrated over the line-emitting channels are presented in Figure 1. The right panel of Figure 1 shows the line spectra integrated within the 2σ contour in the intensity map. We calculate the line widths, redshift, and fluxes of CO(8–7), (9–8), and H_2O by fitting a Gaussian profile to the spectra. We fit a 2D Gaussian component to the intensity maps of CO and H_2O lines, and the source sizes are derived by deconvolving the fitted component with the beam. The spectral profiles of CO(9–8), (8–7), and H_2O are similar (Figure 7), suggesting that the high J CO and H_2O lines are probing similar regions. The source sizes measured from the CO(9–8), (8–7), and H_2O lines of $\approx(0\farcs4 \pm 0\farcs1) \times (0\farcs3 \pm 0\farcs1)$ are slightly smaller than values found from the previous CO(2–1) observation of $(0\farcs6 \pm 0\farcs2) \times (0\farcs4 \pm 0\farcs2)$ and [C II] 158 μm observation of $(0\farcs6 \pm 0\farcs1) \times (0\farcs4 \pm 0\farcs1)$ at similar spatial resolution (Wang et al. 2013; Feruglio et al. 2018; Shao et al. 2019). This may imply that the CO(9–8), (8–7), and H_2O lines trace similar dense molecular regions that are closer to the central SMBH compared to CO(2–1) and [C II] 158 μm. The redshift measured with the CO(9–8), (8–7), and H_2O lines are within the uncertainties consistent with that from previous [C II], CO(2–1), and (6–5) observations (Wang et al. 2013; Feruglio et al. 2018; Shao et al. 2019). The OH^+ line is not as strong as the other detections, so we fix the center frequency to the [C II] 158 μm redshift and fit a Gaussian profile to the spectra extracted from the peak pixel. As for the line widths, all of the ALMA detections show line widths of $\sim$400 km s^{-1} consistent with previous CO and [C II] observations. From the OH^+ spectra, we find that there is an absorption-like feature in the line center frequency, but the current S/N is insufficient to confirm this feature. The continuum detections were published in Shao et al. (2019). The derived continuum source sizes of $\approx(0\farcs30 \pm 0\farcs04) \times (0\farcs22 \pm 0\farcs06)$ are comparable to that measured with the CO and H_2O lines.

We detected CO(5–4), (6–5), (12–11), and (13–12) with NOEMA. All four CO lines are unresolved. For the line widths, redshift, and fluxes calculation, we fit a Gaussian profile to the spectra extracted from the peak intensity pixel. The redshift measured with the CO(5–4), (6–5), (12–11), and (13–12) are consistent with our ALMA detections as well as previous CO and [C II] detections. The line widths detected in ALMA and NOEMA observations are consistent. The CO(6–5) line has been previously detected with ALMA and the (pre-NOEMA) IRAM Plateau de Bure Interferometer (PdBI) with different spatial resolutions and the spectral line flux measured with ALMA is found to be only 70% of that found with the PdBI (Wang et al. 2013; Feruglio et al. 2018). In addition to the calibration uncertainties in different observations, it is also possible that the low resolution PdBI data include more flux from the extended region. The new NOEMA observation yield a CO(6–5) flux of 1.05 ± 0.07 Jy km s^{-1}, consistent with the results obtained with ALMA (Feruglio et al. 2018). We also detected the underlying continuum at high S/N. The measurements of redshift, line widths, line fluxes, and deconvolved source sizes of our ALMA and NOEMA observations as well as previous detections are summarized in Table 2, and the continuum measurements are listed in Table 3. The continuum, line intensity maps, and spectra of CO(5–4), (6–5), (8–7), (9–8), (12–11), (13–12), H_2O, and OH^+ are shown in Figures 2 (NOEMA) and 1 (ALMA).

Figure 3 shows the velocity and velocity dispersion maps of [C II] 158 μm (Wang et al. 2013), CO(8–7), (9–8), and H_2O. The velocity fields of CO(8–7), (9–8), and H_2O overall follow the velocity gradient observed in [C II] 158 μm from north to south, which indicates that the emission might trace a rotating molecular gas disk. The velocity field of CO(8–7) shows a high-velocity dispersion part in the western part, which is not observed in CO(9–8) and H_2O. Such irregular velocity structure in CO(8–7) is likely to be a result of the low S/N. As for the velocity dispersion, CO(8–7), (9–8), and H_2O show velocity dispersion of $<$100 km s^{-1} in the outskirts (that is not likely influenced much by the beam smearing effect). Higher S/N observations, possibly at even higher angular resolution, are required in order to constrain the kinematic structures of the dense molecular gas.

4. Radiative Transfer Analysis of the CO SLED

In the CO SLED analysis, we also include a new detection of the CO (10–9) line from NOEMA at high S/N. More details of the observation will be described in Riechers et al. (2020, in preparation). Our ALMA and NOEMA data, together with previous detections of the CO(2–1) (Shao et al. 2019) and the CO(10–9) emission line, enable us to probe the the CO SLED

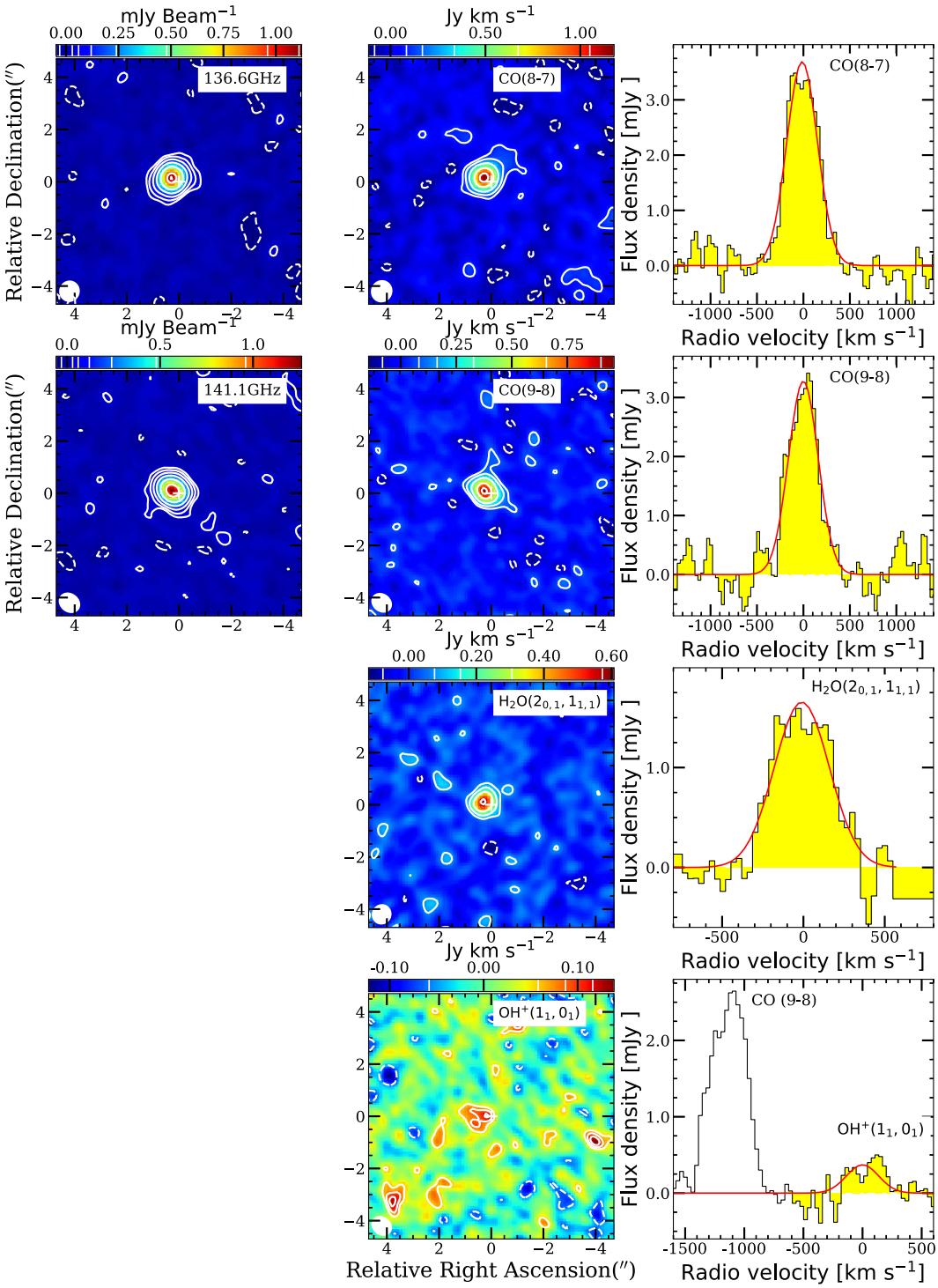

Figure 1. Continuum, line intensity maps, and spectrum (from left to right) of CO(8–7), (9–8), $H_2O(2_{0,2}–1_{1,1})$, and $OH^+(1_1–0_1)$ (from top to bottom) observed by ALMA. The white cross represents the *Gaia* position of the quasar (Shao et al. 2019). The size of the white cross demonstrates the astrometric uncertainty of the quasar position. The filled white ellipse on the lower left shows the FWHM of the beam. First column: continuum maps. The white contours denote [−2, 2, 4, 8, 16, 32, 64, 74] × σ ($1\sigma = 15$ μJy beam^{-1}) at 136.6 GHz and [−2, 2, 4, 8, 16, 32, 64] × σ ($1\sigma = 15$ μJy beam^{-1}) at 141.1 GHz. Second column: spectra line intensity maps. The white contours denote [−2, 2, 4, 8, 16, 25] × σ ($1\sigma = 0.042$ mJy beam^{-1} km s^{-1}), [−2, 2, 4, 8, 16, 22] × σ ($1\sigma = 0.041$ mJy beam^{-1} km s^{-1}), [−2, 2, 4, 8, 15] × σ ($1\sigma = 0.038$ mJy beam^{-1} km s^{-1}) and [−2, 2, 3, 4] × σ ($1\sigma = 0.029$ mJy beam^{-1} km s^{-1}) for CO(8–7), (9–8), $H_2O(2_{0,2}–1_{1,1})$ and $OH^+(1_1–0_1)$ respectively. Third column: the yellow histogram represents the spectra extracted from the 2σ contour on the intensity map for spatially resolved CO(8–7), (9–8), $H_2O(2_{0,2}–1_{1,1})$ lines, and from the peak pixel for spatially unresolved $OH^+(1_1–0_1)$ emission. The red solid line is a single Gaussian profile fit to the spectral line. The Gaussian fit to the $OH^+(1_1–0_1)$ spectral line should be taken with caution since there are possibly both emission and absorption features, and the current sensitivity is not enough to confirm these features. The spatial offsets between the continuum and spectra line emissions are within the uncertainty of the quasar position.

of J2310+1855 from $J = 2$ to $J = 13$, making it the most complete CO SLED ever obtained for a $z \gtrsim 6$ quasar. We here use the radiative transfer model MOLPOP-CEP to investigate the physical conditions of the molecular gas, including the kinetic temperature $T_{\rm kin}$, molecular hydrogen density $n(\rm H_2)$, and CO column density $N(\rm CO)$.

Table 2
Spectral Line Observations

Line	$z_{\rm line}$	FWHM (km s^{-1})	Sδv (Jy km s^{-1})	Beam Size (arcsec)	Source Size (arcsec)	Luminosity ($10^9\,L_\odot$)	Facilities	References
(1)	(2)	(3)	(4)	(5)	(6)	(7)	(8)	(9)
CO(2–1)	6.0029 ± 0.0005	484 ± 48	0.18 ± 0.02	0.61 × 0.59	(0.60 ± 0.18) × (0.40 ± 0.21)	0.021 ± 0.002	VLA	S19
CO(5–4)	6.0030 ± 0.0004	409 ± 44	0.89 ± 0.09	1.67 × 1.37	⋯	0.254 ± 0.026	NOEMA	L19
CO (6 − 5)	6.0025 ± 0.0007	456 ± 64	1.52 ± 0.13	5.4 × 3.9	⋯	0.520 ± 0.045	PdBI	W13
CO(6–5)	6.0028 ± 0.0003	361 ± 9	1.12 ± 0.06	0.6 × 0.4	(0.33 ± 0.06) × (0.20 ± 0.04)	0.383 ± 0.021	ALMA	F18
CO(6–5)	6.0030 ± 0.0003	422 ± 30	1.05 ± 0.07	1.42 × 1.19	(0.74 ± 0.34) × (0.46 ± 0.28)	0.359 ± 0.024	NOEMA	L19
CO(8–7)	6.0028 ± 0.0001	390 ± 15	1.53 ± 0.05	0.79 × 0.75	(0.46 ± 0.09) × (0.21 ± 0.10)	0.699 ± 0.023	ALMA	L19
CO(9–8)	6.0031 ± 0.0002	376 ± 18	1.31 ± 0.06	0.77 × 0.63	(0.41 ± 0.10) × (0.32 ± 0.11)	0.673 ± 0.030	ALMA	L19
CO(10–9)	⋯	⋯	1.04 ± 0.17	⋯		0.594 ± 0.097	⋯	Rpr
CO(12–11)	6.0030 ± 0.0008	451 ± 81	0.78 ± 0.13	2.08 × 1.62	⋯	0.534 ± 0.089	NOEMA	L19
CO(13–12)	6.0028 ± 0.0007	324 ± 75	0.49 ± 0.11	1.91 × 1.53	⋯	0.363 ± 0.082	NOEMA	L19
H_2O	6.0028 ± 0.0003	398 ± 28	0.70 ± 0.05	0.72 × 0.68	(0.39 ± 0.14) × (0.25 ± 0.21)	0.343 ± 0.024	ALMA	L19
OH^+	⋯	320 ± 313	0.13 ± 0.10	0.77 × 0.63	⋯	0.067 ± 0.051	ALMA	L19
$[CII]_{158\mu m}$	6.0031 ± 0.0002	393 ± 21	8.83 ± 0.44	0.72 × 0.51	(0.55 ± 0.05) × (0.40 ± 0.07)	8.310 ± 0.414	ALMA	W13

Note. Column 1: Line ID; Columns 2–4: Redshift, linewidth in FWHM and line flux. Note that the line flux is calculated trough a single Gaussian fit to the line profile; Column 5: Beam size in FWHM; Column 6: Source size deconvolved from the beam in FWHM; Column 7: Line luminosity, and calibration uncertainties are not included in the error bars; Column 8: Facilities; Column 9: References: This paper (L19); Shao et al. (2019) (S18); Wang et al. (2013) (W13); Feruglio et al. (2018) (F18), Riechers et al. (2020, in preparation) (Rpr).

Table 3
Continuum Properties

Frequency (GHz)	Sν (mJy)	Rms (uJy beam^{-1})	Beam Size (arcsec)	Source Size (arcsec)
(1)	(2)	(3)	(4)	(5)
80.6	0.22 ± 0.04	16	1.68 × 1.37	(1.59 ± 0.52) × (0.21 ± 0.45)
96.0	0.29 ± 0.03	15	1.42 × 1.19	(0.83 ± 0.25) × (0.31 ± 0.39)
136.6	1.28 ± 0.03	15	0.75 × 0.72	(0.34 ± 0.04) × (0.22 ± 0.06)
141.1	1.42 ± 0.03	15	0.80 × 0.65	(0.27 ± 0.03) × (0.22 ± 0.06)
200.9	3.88 ± 0.04	45	2.06 × 1.62	⋯
215.9	4.46 ± 0.05	45	1.92 × 1.54	⋯

Note. Column 1: continuum frequency in observed frame; Columns 2–3: continuum flux density and rms; Columns 4–5: beam size and source size deconvolved from beam in FWHM.

4.1. Method

MOLPOP-CEP is a universal code that enables exact solutions of multi-level line emissions radiative transfer problems for all of the atoms/molecules that have atomic/molecular data in the Leiden Atomic and Molecular Database database (Elitzur & Asensio Ramos 2006; Asensio Ramos & Elitzur 2018). This code assumes a slab geometry with the emitting region divided into several zones and treats the radiative transfer problem with a coupled escape probability (CEP) method that aims to solve the coupled level population equations of different zones under consideration. Dividing the geometry into several zones makes it possible to solve the level populations as a function of depth into the line-emitting region and also leads to more accurate solutions compared to previous large velocity gradient models.

The physical parameters as inputs control the number of zones into which the geometry is divided and the physical parameters of the individual zone in the slab geometry. Even for a uniform physical parameter setup in the whole geometry, the division of geometry into zones is necessary to increase the accuracy of the results. This is because, for optically thick lines, the strength of radiative reactions changes with distances to the surface, and the transition level population distributions depend on positions in the geometry (Asensio Ramos & Elitzur 2018). In the slab, each zone in principle can have different physical parameter setups including: (1) the zone width ΔL, (2) the gas density within the zone $n(H_2)$, (3) kinetic temperature $T_{\rm kin}$, (4) molecular abundance, and (5) local linewidth (which corresponds to the line absorption/emission profile in each point in the geometry). In addition to these, MOLPOP-CEP allows the inclusion of an external radiation field. Given these physical parameters, the code will then solve the coupled level population problem between zones and finally predict the emergent intensities of the emission lines that can be directly compared to the observations. We assume uniform parameters for each slab. The accuracy of MOLPOP-CEP solutions increases with the number of zones. Here, we divide the geometry into 10 zones for the model calculation, as is suggested by Asensio Ramos & Elitzur (2018).

We generate a grid of slab models through varying the physical parameters of greatest interest—the gas density $n(H_2)$, temperature $T_{\rm kin}$, and zone width ΔL. For the other two zone parameters, we fix the molecular abundance of CO to $X_{\rm CO} = 10^{-4}$ (Milky Way, Blake et al. 1987), and local linewidth to 1 km s^{-1} for all of the model calculations. In addition, we include the CMB at the quasar redshift of 19.12 K, because the hot CMB at high-redshift will (1) act as an extra heating source of the CO emission, and (2) serve as a continuum background (Da Cunha et al. 2013;

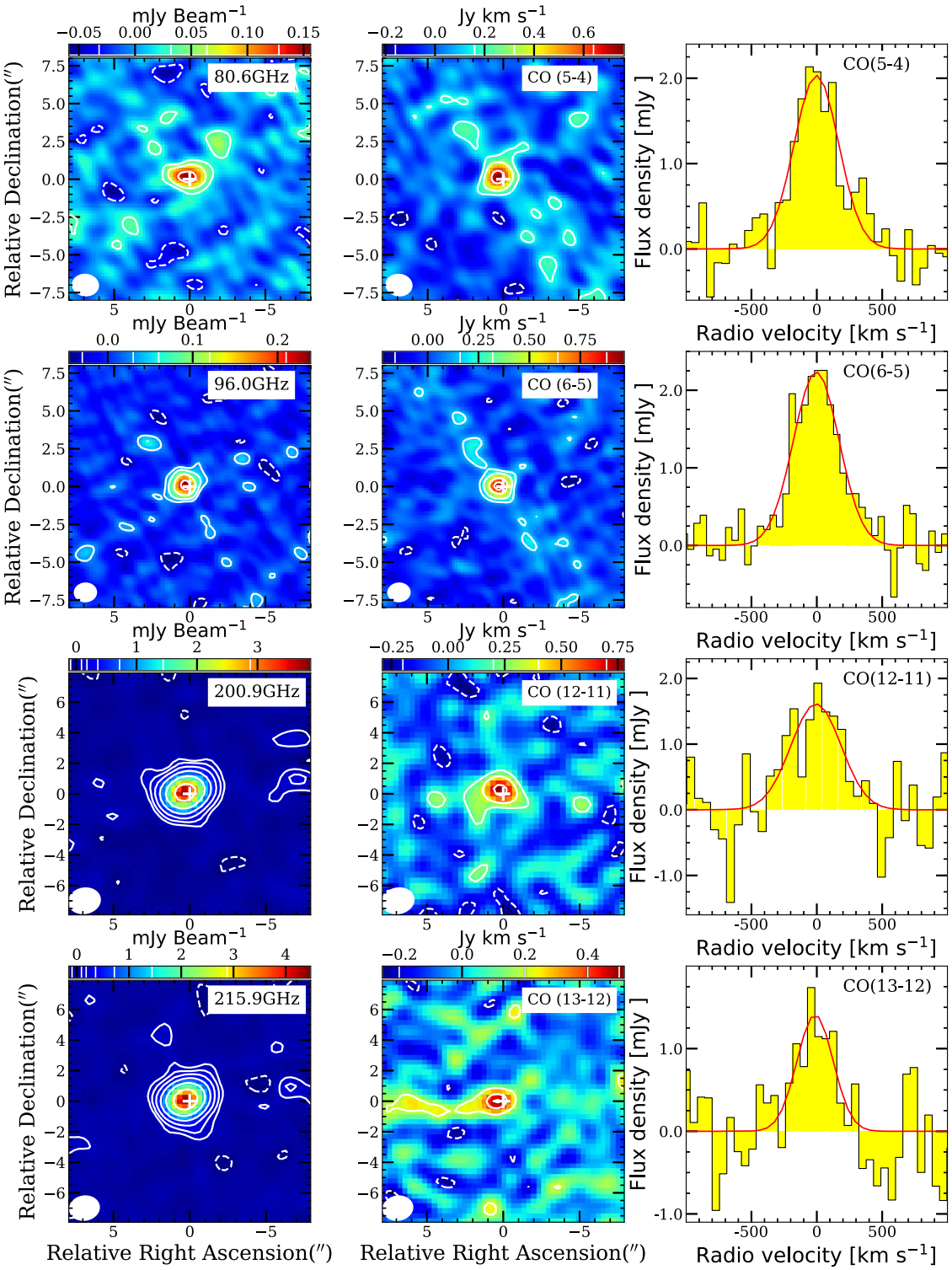

Figure 2. Continuum, line intensity maps, and spectrum (from left to right) of CO(5–4), (6–5), (12–11), and (13–12) (from top to bottom) observed by NOEMA. The white cross on continuum and line intensity map represents the *Gaia* position of the quasar (Shao et al. 2019). The size of the white cross demonstrates the quasar location astrometric uncertainty. The filled white ellipse on the lower left shows the FWHM of the beam. For the continuum maps (first column), contours denote [−2, 2, 4, 8] × σ (1σ = 16 μJy beam^{-1}) at 80.6 GHz, [−2, 2, 4, 8, 14] × σ (1σ = 15 μJy beam^{-1}) at 96.0 GHz, [−2, 2, 4, 8, 16, 32, 64] × σ (1σ = 45 μJy beam^{-1}) at 200.9 GHz and [−2, 2, 4, 8, 16, 32, 64] × σ (1σ = 45 μJy beam^{-1}) at 215.9 GHz. For the spectra line intensity maps (second column), contours denote [−2, 2, 4, 8, 10] × σ (1σ = 0.08 mJy beam^{-1} · km s^{-1}), [−2, 2, 4, 8, 11] × σ (1σ = 0.08 mJy beam^{-1} km s^{-1}), [−2, 2, 4, 7] × σ (1σ = 0.10 mJy beam^{-1} km s^{-1}) and [−2, 2, 4, 5] × σ (1σ = 0.10 mJy beam^{-1} · km s^{-1}) for CO(5–4), (6–5), (12–11), and (13–12), respectively. Third column: yellow histogram represents spectrum extracted from the peak pixel (all spectra lines are spatially unresolved), and the red solid line is a single Gaussian profile fit to the spectral line. The peak positions of the continuum and spectra line emissions are within uncertainty of the quasar position.

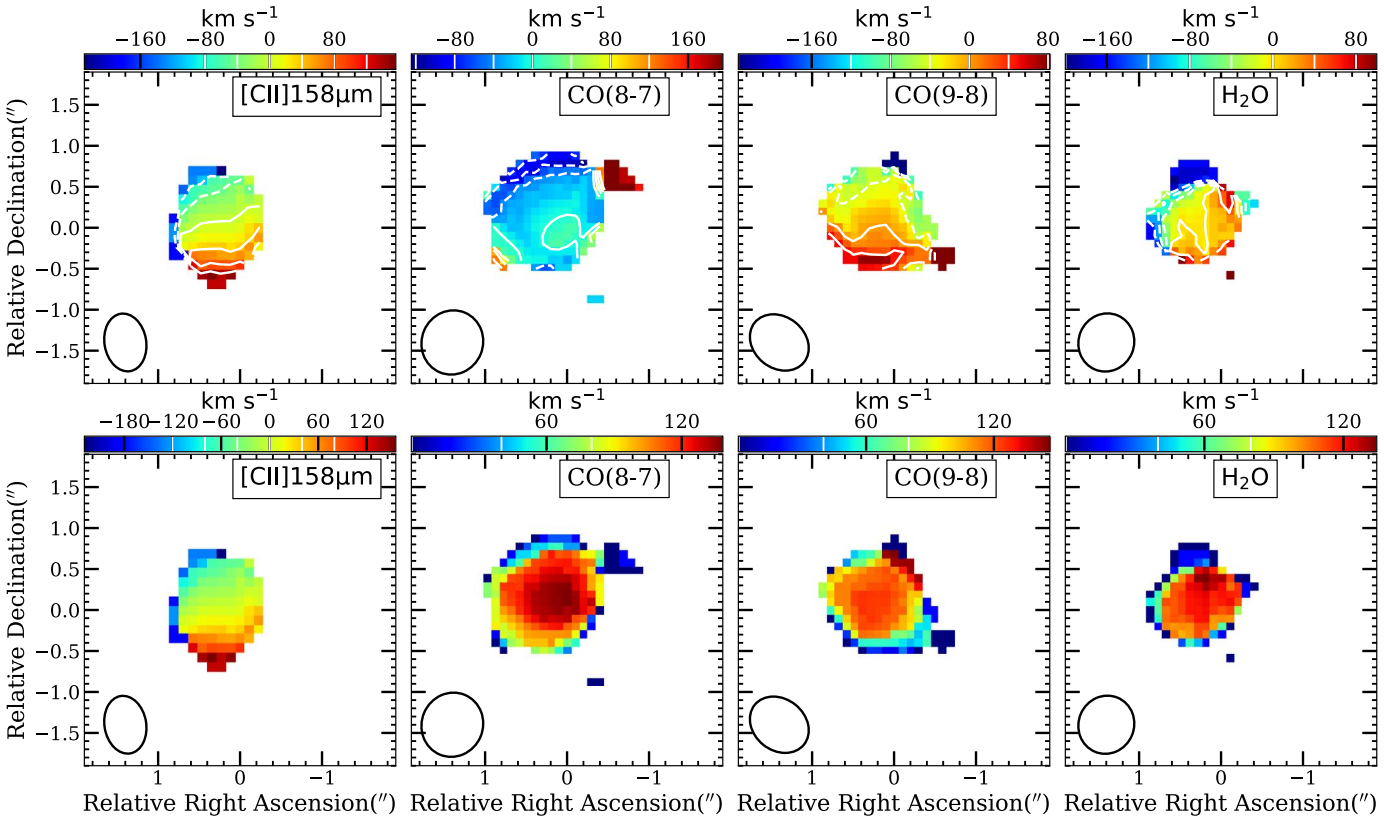

Figure 3. Velocity (first row) and velocity dispersion (second row) of [C II]158 μm, CO(8–7), (9–8), and $H_2O(2_{0,2}–1_{1,1})$ (left to right). The black ellipse on the left shows the FWHM of the beam. We generate the velocity and velocity dispersion maps with the pixels of $\geqslant 3.0\sigma$ values in the line-emitting channels, and the zero velocity corresponds to the [C II]158 μm redshift of 6.0031 (Wang et al. 2013). The white contours on the velocity maps are $[-4, -2, 0, 2, 4, 6] \times 20$ km s^{-1} for [C II]158 μm, $[-6, -4, -2, 0, 2, 4, 6] \times 20$ km s^{-1} for CO(8–7), $[-6, -4, -2, 0, 2, 4] \times 20$ km s^{-1} for CO(9–8), and $[-6, -4, -2, 0, 2, 4] \times 20$ km s^{-1} for $H_2O(2_{0,2}–1_{1,1})$. We find in the velocity maps that CO(8–7), (9–8), and $H_2O(2_{0,2}–1_{1,1})$ generally follow the velocity gradient observed from [C II]158 μm (Wang et al. 2013) from northeast to southwest.

Zhang et al. 2016). In each model, all 10 zones have the same physical parameter setup; thus, each model in the grid can be described by a uniform $n(H_2)$, T_{kin} and ΔL. The CO column density within the geometry, which is the sum of the column densities of 10 zones, is proportional to the zone width ΔL through:

$$N(\mathrm{CO}) = 10 \times n(\mathrm{H_2}) \times \Delta L \times X_{\mathrm{CO}}. \quad (1)$$

In the remainder of the paper, we use $n(H_2)$, T_{kin}, and $N(CO)$ to characterize the physical condition of each slab grid. As it is easier to use $N(CO)$ rather than ΔL to make comparisons with constraints from observations (see Section 4.2). The final grid covers the typical physical conditions of the molecular clouds with a temperature range of 20–800 K, density of 10^3–10^8 cm^{-3}, and CO column density of 10^{14}–10^{21} cm^{-2} (this corresponds to a H_2 column density of 10^{18}–10^{25} cm^{-2} for our assumed X_{CO} of 10^{-4}). More details about the grid are listed in Table 4.

We use the model grid to fit our observed CO SLED of J2310+1855. The fitting procedure is as follows: we first apply the least-squares method to find the best-fitting results. We also use the Bayesian code emcee (Foreman-Mackey et al. 2013) to efficiently explore the parameter space and get the posterior probability distributions of all parameters considered. Emcee is an extensible, pure-Python implementation that is designed for Bayesian parameter estimation using Ensemble samplers with affine invariance (Goodman & Weare 2010).

4.2. Parameter Constraints

During the fitting procedure, we set constraints for the three parameters: T_{kin}, $n(H_2)$, and $N(CO)$. The fact that T_{kin} is hotter than the background CMB radiation at redshift 6 is a prior, which sets $T_{kin} > 19.12$ K. As for column density, one prior is that the total amount of gas producing the observed CO luminosities should be no more than the total dynamical mass of this system, this leads to:

$$N(\mathrm{CO})\Phi_A < \frac{M_{\mathrm{dyn}} X_{\mathrm{CO}}}{\mu m_{\mathrm{H2}} A}\ [\mathrm{cm^{-2}}], \quad (2)$$

where Φ_A is the filling factor, M_{dyn} is the dynamic mass, A is the source area in cm^2, ΔV is the CO linewidth in km s^{-1}, μ is the mean molecular weight, m_{H2} is the H_2 molecule mass, and X_{CO} is the CO abundance. The source size and gas dynamical mass are adopted from Shao et al. (2019), with $M_{dyn} \approx 4.3 \times 10^{10} M_\odot$ and $A \approx \frac{\pi}{4} \times 0.60 \times 0.40$ arcsec^2. Adopting a CO-to-H_2 abundance ratio $X_{CO} = 10^{-4}$, and $\mu = 1.4$ for mean molecular weight, the final constraint is:

$$N(\mathrm{CO})\Phi_A < 3.2 \times 10^{19}\ [\mathrm{cm^{-2}}]. \quad (3)$$

The other prior for column density is that it should be less than the source gas volume density integrated along the line of sight for line-emitting regions. This leads to:

$$N(\mathrm{CO}) < n(\mathrm{H_2}) \times X_{\mathrm{CO}} \times S\ [\mathrm{cm^{-2}}], \quad (4)$$

Table 4
MOLPOP-CEP Grid Parameter Ranges

Input Parameters (1)	Range (2)	Grid Step (3)	Grid Number (4)	Unit (5)
Kinetic Temperature ($T_{\rm kin}$)	20–800	$\Delta T_{\rm kin} = 13$	61	K
Volume Density ($n(\rm H_2)$)	10^3–10^8	$\Delta{\rm Log}(n_{\rm H2}/{\rm cm}^{-3}) = 0.25$	21	$\rm cm^{-3}$
Column Density (N(CO))	10^{14}–10^{21}	$\Delta{\rm Log}(N_{\rm CO}/{\rm cm}^{-2}) = 0.5$	15	$\rm cm^{-2}$

Note. Column 1: input parameters to generate the grid; Column 2: parameter ranges; Column 3: steps of parameters in log space; Column 4: the resulting number of grid for a specific parameter; Column 5: units

where S is the source size along the line of sight, and $n(\rm H_2)$ is the $\rm H_2$ volume density. Assuming a largest diameter of CO-emitting region of 0.″60 (Shao et al. 2019), we set a constraint on both N(CO) and $n(\rm H_2)$ as follows:

$$\frac{N({\rm CO})}{n({\rm H_2})} < 1.1 \times 10^{18}[{\rm cm}]. \quad (5)$$

4.3. Fitting Results

We endeavor to probe the physical conditions of the molecular gas in J2310+1855 by fitting a one-component model to the CO SLED. Calibration uncertainties are included in all of the modeling processes throughout the paper. We first fit the grid models to the observed CO SLED with the least-squares method. The left panel of Figure 4 shows the best-fitting result, suggesting a "warm" and "dense" gas component with kinetic temperature of $T_{\rm kin} = 228$ K, density of $\log(n({\rm H_2})/{\rm cm}^{-3}) = 4.75$, and column density of $\log(N({\rm CO})/{\rm cm}^{-2}) = 17.5$. We then search for all possible physical conditions that fit the observational CO SLED with the emcee code. The posterior probability distributions of the three parameters are shown in Figure 5. This indicates that the data can be fitted with a "warm" and "dense" gas component with parameter range of $T_{\rm kin} \approx 167^{+153}_{-56}$ K, $\log(n({\rm H_2})/{\rm cm}^{-3}) \approx 5.11^{+1.83}_{-0.58}$, and $\log(N({\rm CO})/{\rm cm}^{-2}) \approx 17.28^{+0.33}_{-0.42}$.[18] But the current best-fit model fails to reproduce the very high CO(8–7) line flux detected.

Previous CO SLED modeling from local to high-redshift galaxies/AGNs suggest different gas physical properties in different systems. Exempli gratia in the $z = 2.56$ quasar cloverleaf (Riechers et al. 2011) and the $z = 6.34$ starburst galaxy HLFS3 (Riechers et al. 2013), a single gas component is able to reproduce the observed CO SLED. In addition, more than one gas component is found in the CO SLED analysis of local starburst galaxies, (U)LIRGs, and even the quasars at the highest redshift (e.g., M82, NGC 1068, Mrk 231, APM 08279+5255, J0100+2802, J0439+1634, and J1148+5251 (Weiß et al. 2005, 2007; Panuzzo et al. 2010; van der Werf et al. 2010; Spinoglio et al. 2012; Gallerani et al. 2014; Wang et al. 2019a; Yang et al. 2019)). The CO SLED of the $z = 6.3$ quasar J0100+2802 suggests two components of gas, with a "cold" component with $T_{\rm kin} \approx 24$ K, $\log(n({\rm H_2})/{\rm cm}^{-3}) \approx 4.5$ and a "warm" component with $T_{\rm kin} \approx 224$ K, $\log(n({\rm H_2})/{\rm cm}^{-3}) \approx 3.6$ (Wang et al. 2019a). The CO SLED of J0439+1634 at $z = 6.5$ indicates a "cold" component with $T_{\rm kin} \approx 23$ K and $\log(n({\rm H_2})/{\rm cm}^{-3}) \approx 4.1$ in combination with a "warm" component with $T_{\rm kin} \approx 140$ K and $\log(n({\rm H_2})/{\rm cm}^{-3}) \approx 4.5$ (Yang et al. 2019). The cold component was thought to be associated with the sub-mm/mm-detected dust component powered by active star formation with temperatures of $40 \sim 60$ K (assuming optically thin; Beelen et al. 2006; Leipski et al. 2013). The dust continuum SED fitting of J2310+1855 indicates a dust temperature of ~40 K in the optically thin dust assumption of Shao et al. (2019) or 76 K in the optically thick assumption of Carniani et al. (2019). Both are much lower than the one-component fitting result of $T_{\rm kin} = 228$ K. As the one-component best-fit model fails to explain the observed CO (8–7) flux (left panel of Figure 4), it is possible that there is an additional "cold" gas component physically associated with the sub-mm/mm-detected dust in J2310+1855. Motivated by the above, we examine whether the data can be explained with a two-component model.

The two-component model fitting to the data requires eight parameters, including the physical parameters ($T_{\rm kin}$, $n(\rm H_2)$, and N(CO)) and the normalization of each component. Our data are insufficient to constrain all eight parameters. Considering that the "cold" component is usually physically connected to and has a similar temperature to that of the cold dust (as is explained in detail in the previous paragraph), and the dust temperature of J2310+1855 is not well constrained ($T_{\rm dust}$ ranges between 40 and 80 K depending on the dust model assumed), we will fix the "cold" component to the typical "cold" gas physical conditions observed in $z \sim 6$ quasar in the following analysis. With this assumption, we are fitting only five instead of eight parameters. As a consequence, the model parameters could be better constrained. We adopt a typical "cold" gas component with physical parameters of $T_{\rm kin} \approx 50$ K and $\log(n({\rm H_2})/{\rm cm}^{-3}) = 4.2$ that is observed in a "typical" $z \sim 6$ quasar J1148+5251 (Riechers et al. 2009). Because column density is not one of the model parameters in Riechers et al. (2009), we use a column density of $\log(N({\rm CO})/\,{\rm cm}^{-2}) = 18.0$ for the "cold" model. We note that the resulting $X_{\rm CO}/dv/dr$ here is different from that in Riechers et al. (2009), because in the MOLPOP-CEP model, the dv/dr is derived from the first principle and is different in different places in the whole geometry. The final "cold" model using the set of parameters we adopted here can well represent the observational CO SLED of J1148+5251 presented in Riechers et al. (2009). The right panel of Figure 4 shows the minimum χ^2 fitting result of the two-component model. The resulting "warm" component with the minimum χ^2 has a physical condition of $T_{\rm kin} = 306$ K, $\log(n({\rm H_2})/{\rm cm}^{-3}) = 5.25$, and $\log(N({\rm CO})/{\rm cm}^{-2}) = 15.5$. We find in the fitting result that the "cold" component (the J1148+5251 model) dominates the low J ($J = 2$) part and contributes to 77% of the observed CO(2–1) flux. As we have already mentioned before, the low J CO emission lines trace the total molecular gas mass; thus, the "cold" component dominates the total molecular gas mass. In the mid-J ($J = 5$, 6) part, the contribution of the "cold" component decreases and only accounts for ~30% of the observed CO fluxes. And in the high J ($J \geqslant 8$) part, the "cold"

[18] The resulting parameter ranges are consistent within 1σ between including and excluding the CO(10–9) line in the fitting procedure.

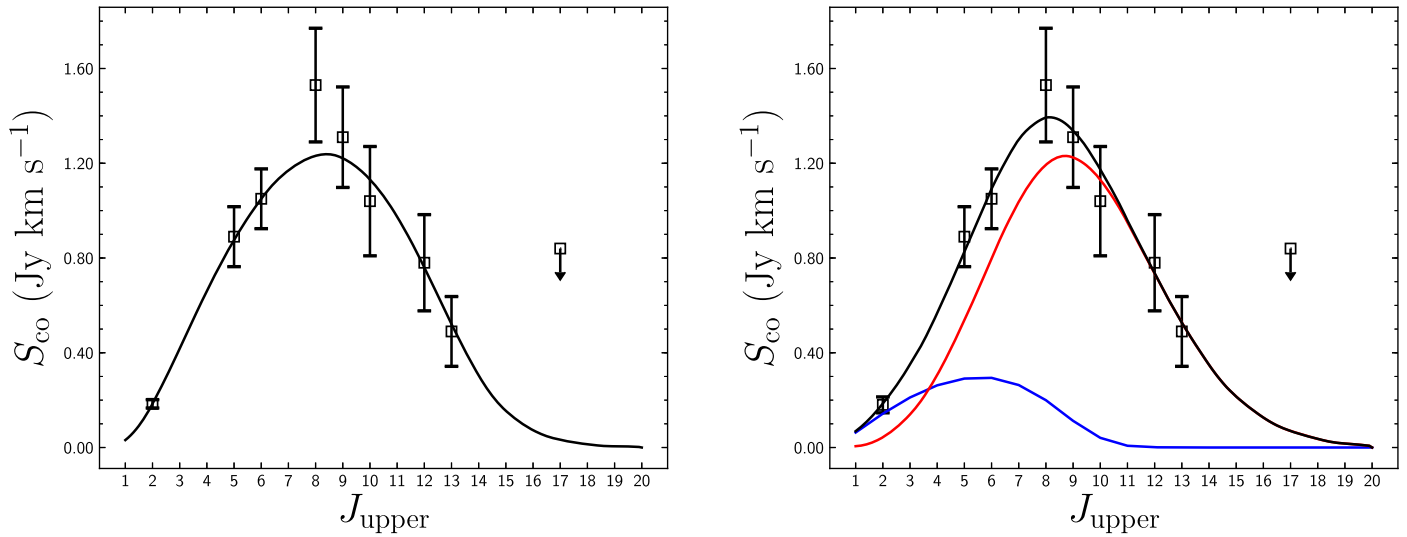

Figure 4. CO SLED fitted with one- (left panel) or two-component (right panel) models. The black squares are the CO fluxes of J2310+1855 with the calibration uncertainties included. The CO(5–4), (6–5), (8–7), (9–8), (12–11), and (13–12) data are from this work. The CO(2–1) data is taken from Shao et al. (2019), the CO(10–9) data will be presented in Riechers et al. (2020, in preparation), and the upper limit of the CO(17–16) line is from Carniani et al. (2019). Details are presented in Table 2. Left panel: the black solid line represents the best one-component fitting result with the minimum χ^2 ($T_{\rm kin}$ = 228 K, $\log(n({\rm H_2})/{\rm cm^{-3}}) = 4.75$, and $\log(N({\rm CO})/{\rm cm^{-2}}) = 17.5$). Right panel: least-squares fitting result with two-component model. The blue solid line represents the J1148+5251 model with $T_{\rm kin}$ = 50 K, $\log(n({\rm H_2})/{\rm cm^{-3}}) = 4.20$ and $\log(N({\rm CO})/{\rm cm^{-2}}) = 18.0$ (Riechers et al. 2009). The red solid line is the "warm" component with $T_{\rm kin}$ = 306 K, $\log(n({\rm H_2})/{\rm cm^{-3}}) = 5.25$ and $\log(N({\rm CO})/{\rm cm^{-2}}) = 15.5$.

component contribution is negligible. The "warm" component, that barely contributes to the total molecular gas mass, dominates the CO SLED from the mid- to the high-J ($J \geqslant 5$) part of the overall CO SLED. The posterior probability distributions of the parameters calculated by the emcee code are shown in Figure 5. It suggest a "warm" and "dense" component with parameter range of $T_{\rm kin} \approx 306^{+263}_{-149}$ K, $\log(n({\rm H_2})/{\rm cm^{-3}}) \approx 5.22^{+1.04}_{-0.49}$, and $\log(N({\rm CO})/{\rm cm^{-2}}) \approx 15.29^{+1.34}_{-1.17}$.[19]

To summarize, the best one-component "warm" and "dense" model reproduces the observed CO SLED, in general, except for an underestimation of the CO(8–7) flux. The two-component fitting result suggests that the CO SLED at $J \geqslant 5$ is dominated by a "warm" and "dense" gas component, while the "cold" component barely contributes to the mid- to the high-J CO fluxes but dominates the total molecular gas mass. Either the one- or two-component model suggests that the CO SLED detected within the nuclear region (source size of $\sim$2 kpc) of the quasar host is dominated by a "warm" and "dense" gas component at $J \geqslant 5$.

5. Discussion

5.1. CO Emission in J2310+1855 Compared with Local Starburst Systems

The CO SLED reveals the physical conditions of molecular gas (e.g., the illuminating radiation field strength, kinetic temperature, volume density, and column density). We first compare the CO SLED of J2310+1855 with local starburst systems. Figure 6(a) shows the CO SLED of J2310+1855 compared with two local starburst samples. They are local (U)LIRGs sample consisting of 29 (U)LIRGs (Rosenberg et al. 2015) and local normal + starburst galaxy sample consisting of 43 star-forming galaxies (SFGs) and 124 (U)LIRGs (Liu et al. 2015). Although there are actually a small number of AGNs contained in the two (U)LIRGs comparison samples, they are confirmed to impact negligibly on both the CO flux and the infrared luminosity (Rosenberg et al. 2015). For the Rosenberg et al. (2015) sample, we exclude NGC 6240 in a sample mean calculation (because this AGN represents a very extreme CO SLED, see details in Section 5.2). Through comparisons, we find that the peak of the CO SLED is $\lesssim$4 for all local starburst samples, while the J2310+1855 CO SLED peaks at much higher J transitions at $J = 8$. The CO emission lines of J2310+1855 show higher excitation compared to all local (U)LIRG samples (i.e., the CO flux is higher than the average of all local ULIRG samples and is also well above the range of all comparison samples, especially for $J \geqslant 8$). In addition, we compare J2310+1855 with a representative example of local starburst galaxy M82 in Figure 6(b). We get a similar result to that of the starburst samples. The CO SLED of M82 peaks at $J = 5$ and decreases dramatically at $J \geqslant 8$, contrary to J2310+1855, which peaks at $J = 8$ and is luminous even at $J \geqslant 10$.

The high CO excitation detected in the J2310+1855 nuclear region (source size of $\sim$2 kpc in FWHM) may indicate other heating mechanisms besides the UV heating from massive young stars (e.g., mechanical heating by shocks, X-ray heating from AGNs), or very intense UV radiation field (e.g., large UV photon flux produced by a result of both the quasar and the star formation, see Section 5.5 for further discussions about these heating mechanisms).

5.2. CO Emission in J2310+1855 Compared with Local AGNs

We compare the CO emission lines of J2310+1855 with some representative local AGNs (Mrk 231, NGC 1068, and NGC 6240). The AGNs we selected are thoroughly studied local AGNs that represent different CO heating mechanisms. NGC 1068 is one of the closest AGNs, whose high J CO emission lines in the circumnuclear disk (CND) are best explained by an XDR model, and the starburst ring at larger radii that dominates the molecular gas mass is best fitted with a

[19] The resulting parameter ranges are consistent within 1σ between including and excluding the CO(10–9) line in the fitting procedure.

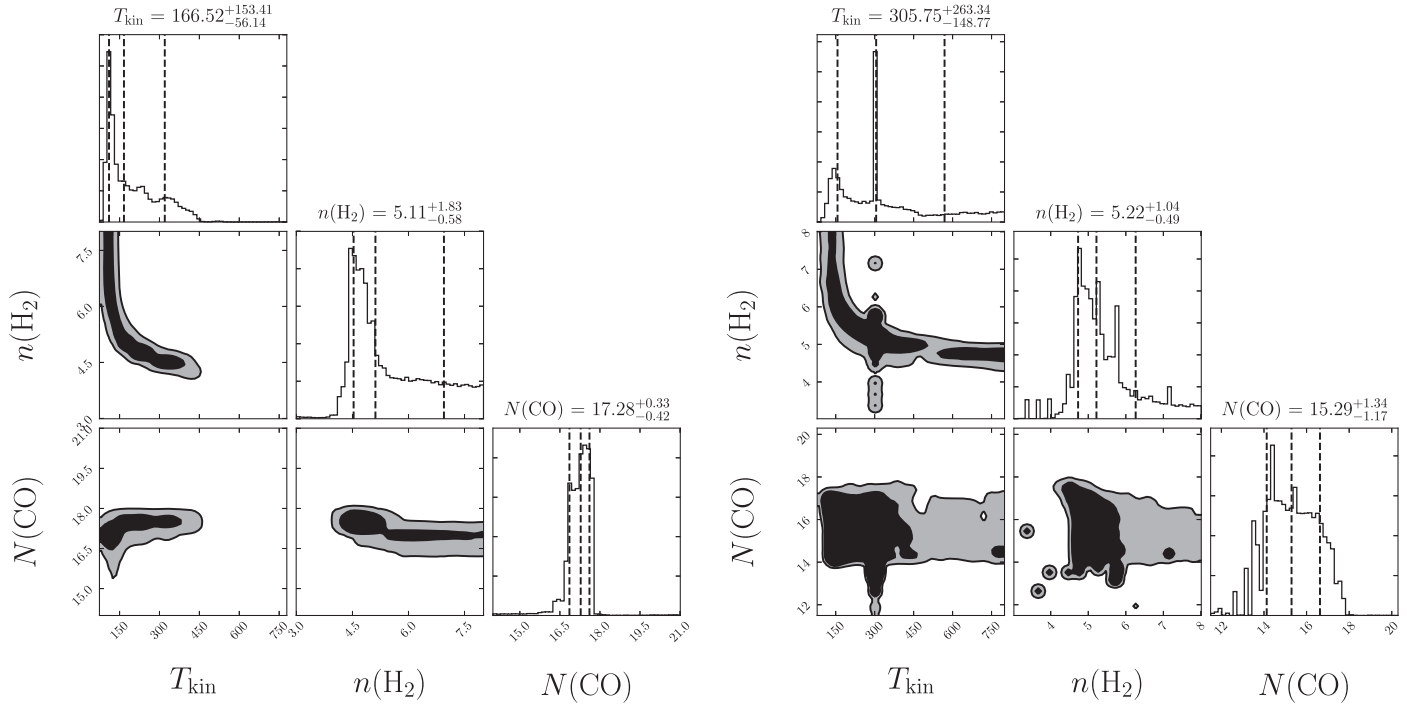

Figure 5. Posterior probability distributions of the three parameters $T_{\rm kin}$ (K), $\log(n(\rm H_2)/\rm cm^{-3})$, and $\log(N(\rm CO)/\rm cm^{-2})$. The plotted contours show the 95% and 68% confidence intervals. Left panel: posterior probability distribution of the parameters for the one-component model. The resulting MCMC result is $T_{\rm kin} \approx 167^{+153}_{-56}$ K, $\log(n(\rm H_2)/\rm cm^{-3}) \approx 5.11^{+1.83}_{-0.58}$, and $\log(N(\rm CO)/\rm cm^{-2}) \approx 17.28^{+0.33}_{-0.42}$. We note that the median and uncertainties here are calculated based on the 16th, 50th, and 84th percentiles of the samples in the marginalized distributions. Right panel: posterior probability distribution of the "warm" component in the two-component model fit to the data. The fitting result suggests the "warm" component with $T_{\rm kin} \approx 306^{+263}_{-149}$ K, $\log(n(\rm H_2)/\rm cm^{-3}) \approx 5.22^{+1.04}_{-0.49}$, and $\log(N(\rm CO)/\rm cm^{-2}) \approx 15.29^{+1.34}_{-1.17}$.

PDR model (Spinoglio et al. 2012). Mrk 231 requires an XDR model to fit the high J CO emission lines in the central 160 pc molecular region, although the low J CO lines are mainly from the PDR component at larger distances (van der Werf et al. 2010). NGC 6240 is a local AGN with three nuclei, the CO emission lines are unlikely to correlate with the position of either AGN nuclei, and mechanical heating is proposed to interpret the extremely excited CO SLED and also the optical ISM emission lines (Meijerink et al. 2013; Kollatschny et al. 2019).

Figure 6(b) shows the CO SLED of J2310+1855 and the local AGNs. The CO SLED of NGC 1068 peaks at $J \leqslant 4$, and then decreases rapidly with increasing J. Mrk 231 shows an extreme CO SLED that peaks at $J = 5$ and displays a high normalized CO flux even at $J \approx 10$–13. The differences between NGC 1068 and Mrk 231 can be explained by different X-ray energy input to the CO heating, evident from the higher X-ray flux derived in Mrk 231 (28 erg cm^{-2} s^{-1}, van der Werf et al. 2010) than NGC 1068 (9 erg cm^{-2} s^{-1}, Spinoglio et al. 2012). NGC 6240 shows the most extreme CO SLED among these three AGNs. The quasar J2310+1855 peaks at higher J ($J = 8$) compared to these local AGNs, i.e., the gas in the nuclear region of J2310+1855 has higher excitation compared to that of the local AGNs.

5.3. CO Emission in J2310+1855 Compared with High-redshift Systems

We also compare the CO SLED of J2310+1855 with high-redshift systems, including high-redshift (lensed) SMGs and quasars. Figure 6(a) shows the CO SLED of J2310+1855 and high-redshift SMGs: a sample of $z \sim 1.2$–4.1 SMGs (Bothwell et al. 2013) and a sample of 15 $z \sim 2$–4 lensed SMGs from Carilli & Walter (2013) and Yang et al. (2017). The high-redshift SMG CO SLEDs peak at $J \lesssim 6$, while J2310+1855 peaks at higher J ($J = 8$) than the two SMG samples. This is similar to the results when comparing the J2310+1855 CO SLED to local starburst samples.

We also select some well-known high-redshift quasars for comparison. Including two lensed quasars, the Cloverleaf at $z = 2.56$ and APM 08279+5255 at $z = 3.91$. The fit to the CO SLED detected in the very central region of APM 08279+5255 requires an XDR component dominating the high J CO emission lines (Bradford et al. 2011). We also include three $z \gtrsim 6$ quasars that are detected in at least four CO transitions: J1148+5251, J0439+1634, and J0100+2802 (Bertoldi et al. 2003; Walter et al. 2003; Beelen et al. 2006; Riechers et al. 2009; Gallerani et al. 2014; Wang et al. 2019a; Yang et al. 2019). Together with J2310+1855, this allows us to perform a systematic study of the CO emission lines in the quasar-starburst systems at the highest redshift. Figure 6(c) shows the CO SLED of J2310+1855 compared to other high-redshift quasars. APM 08279+5255 exhibits the most extreme CO SLED that is detected in the nuclear 550 pc size scale, and it represents a highly excited nuclear CO SLED exposed to the intense X-rays from the quasar. The limited CO detections in J0439+1634 and Cloverleaf suggests that maybe the CO SLED peaks at $J = 8 \sim 10$, similarly to J2310+1855. As for J1148+5251 and J0100+2802, we are not able to determine the CO SLED peak. This is because for J0100+2802, there is no CO observation at $J = 8$, 9 and $J > 11$, while the CO SLED of J1148+5251 is observed at $J \leqslant 7$ and $J = 17$. The comparison of CO SLEDs between J2310+1855 and other high-z quasars suggest that a highly excited molecular gas component is common in the nuclear region of the quasar hosts. However, as

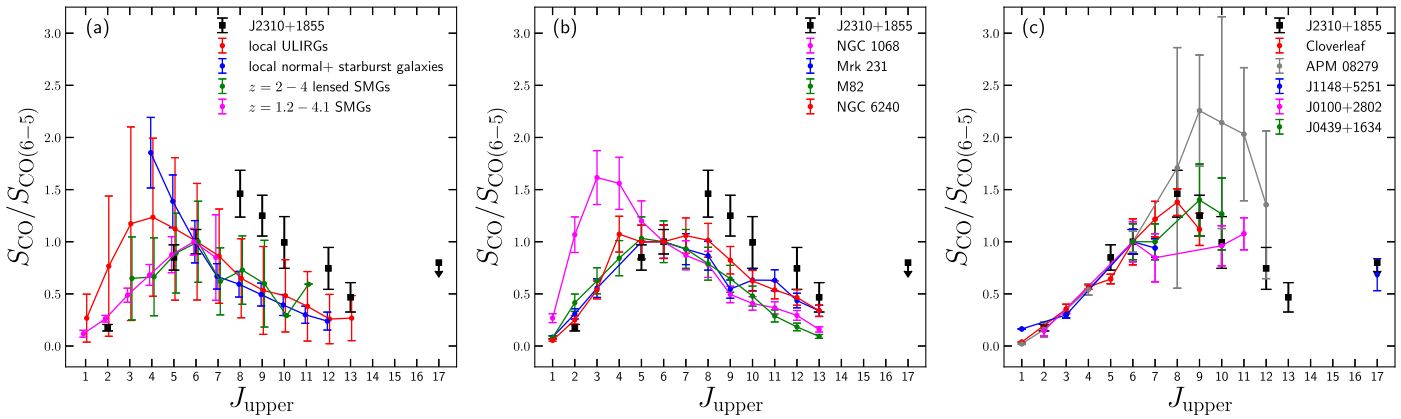

Figure 6. CO SLED normalized to CO(6–5) in normalized unit of Jy km s^{-1}. Left column: J2310+1855 (black squares) in comparison with the mean of four galaxy samples: the local (U)LIRGs (Rosenberg et al. 2015) (red); local normal + starburst galaxies (Liu et al. 2015) (blue); $z \sim 1.2$–4.1 SMGs (Bothwell et al. 2013) (magenta); and strongly lensed SMGs at $z \sim 2$–4 (Yang et al. 2017) (green). Middle column: J2310+1855 (black squares) in comparison with local starburst systems and AGNs. M82 (Weiß et al. 2005; Panuzzo et al. 2010) (green) is a representative example of the local starburst galaxy. The local representative AGNs are NGC 1068 (Spinoglio et al. 2012) (magenta), Mrk 231 (van der Werf et al. 2010) (blue), and NGC 6240 (Rosenberg et al. 2015)(red). Right column: J2310+1855 (black squares) in comparison with high-redshift quasars. The plotted quasars are APM 08279+5255 (Weiß et al. 2007; Riechers et al. 2009; Bradford et al. 2011) (gray), Cloverleaf (Bradford et al. 2009; Uzgil et al. 2016) (red), J1148+5251 (Bertoldi et al. 2003; Walter et al. 2003; Beelen et al. 2006; Riechers et al. 2009; Gallerani et al. 2014) (blue), J0439+1634 (Yang et al. 2019) (green), and J0100+2802 (Wang et al. 2019a) (magenta).

described above, the shape of the CO SLED of these systems are different from object to object. Due to the lensing effect, the CO SLED of APM 08279+5255 may represent molecular gas on <1 kpc scale. The CO SLED of J2310+1855 is not as extreme as APM 08279+5255, and more comparable to the Cloverleaf. When compared to the two $z > 6$ quasars, J0100+2802 and J0439+1634, that have available CO data at $J = 8 \sim 11$, J2310+1855 is more single-peaked no flatten or turn over around $J = 6$. It is possible that the cold star-forming component contribute more to the flux of the mid-J CO in the cases of J0100+2802 and J0439+1634.

5.4. H_2O and OH^+ Emission

Recent studies found linear relations between the infrared luminosity and the $H_2O(2_{0,2}–1_{1,1})$ luminosity in local and high-redshift infrared bright systems, suggesting that the excitation of this water transition is dominated by infrared pumping (van der Werf et al. 2011; Yang et al. 2016; Jarugula et al. 2019). We first compare the H_2O detection of J2310+1855 to the local and high-redshift (U)LIRGs. Figure 7 shows the L_{H_2O} and L_{IR} for local and high-redshift (U/Hy)LIRGs and AGNs. The black dashed line is the best fit to the local and high-redshift (U/Hy)LIRGs presented in Figure 3 of Yang et al. (2016). We consider the infrared luminosity of J2310+1855 in two cases: (1) we adopt total infrared luminosity from both the quasar and the host galaxy ($L_{IR(total)}$); (2) we use the infrared luminosity only from the host galaxy ($L_{IR(galaxy)}$, Shao et al. 2019). The linear relation is fitted with (U/Hy)LIRGs (local and high z) and dusty star-forming galaxies, while all four plotted AGNs including J2310+1855 are well below this relation. This is because the AGNs not only provide the power source of water emission but also contribute significantly to the infrared luminosity (González-Alfonso et al. 2010; van der Werf et al. 2011). As for the host galaxy infrared luminosity case, J2310+1855 reveals a slightly higher water luminosity given its galaxy IR luminosity compared to the linear relation. The velocity dispersion map of the H_2O shows a velocity dispersion of <100 km s^{-1}, suggesting that it may not be the large velocity dispersion that contributes to the luminous water emission. Higher spatial resolution observations are required to confirm this. We find in J2310+1855 a slightly higher L_{H_2O}/L_{IR} ratio than that for local and high-redshift (U/Hy)LIRGs. At $z \sim 6$, only a few quasars are detected in water emission (Bañados et al. 2015; Yang et al. 2019). A similar result is found in the $z = 6.52$ quasar J0439+1634, where a higher $L_{H_2O(3_{2,1}-3_{1,2})}/L_{IR}$ ratio is found as compared to the linear relation (Yang et al. 2019).

To further investigate the heating sources of molecular gas, we also study the ratio between H_2O and CO in J2310+1855. Extremely luminous H_2O emission is not expected in typical PDRs. Exempli gratia, in the Orion bar (a representative dense PDR with $n \sim 10^5$ cm^{-3} illuminated by an intense FUV radiation field of $G_0 = 4 \times 10^4$), the $L_{H_2O}/L_{CO\ (6-5)}$ ratio is 0.20 (Habart et al. 2010; Putaud et al. 2019). Another example is the local starburst galaxy M82, which shows a ratio of 0.06 (Kamenetzky et al. 2012). If the physical/chemical condition is dominated by shocks or X-rays, then the $L_{H_2O}/L_{CO\ (6-5)}$ ratio can even be as high as unity. NGC 1266 is an S0 galaxy highly excited in molecular gas, and Pellegrini et al. (2013) found an $L_{H_2O}/L_{CO\ (6-5)}$ ratio of 0.96 that can be only explained by shocks. Mrk 231 is representative of the molecular gas heated by X-rays, and it has an $L_{H_2O}/L_{CO\ (6-5)}$ ratio of 1.10 ± 0.17 (González-Alfonso et al. 2010). The quasar J2310+1855 exhibits an $L_{H_2O}/L_{CO\ (6-5)}$ ratio of 0.97 ± 0.09, which is comparable to Mrk 231 and NGC 1266 but is much higher than Orion bar and M82. These suggest that the molecular gas heating is not likely dominated by PDR. In addition, we also consider the high-redshift lensed SMGs for comparison (Omont et al. 2013; Yang et al. 2013, 2016, 2017). These lensed SMGs are all starbursts that are exposed to intense radiation field and shocks, and some have extremely luminous water emission lines that cannot be purely explained by PDR. For the majority of the SMGs, the $L_{H_2O}/L_{CO\ (6-5)}$ ratio is found to be less than 0.8, while only quite a few objects have ratios of ∼1, which is unlikely PDR. The even higher $L_{H_2O}/L_{CO\ (6-5)}$ ratio of J2310+1855 compared to typical high-redshift lensed SMGs might suggest additional gas heating by the central luminous quasar. We also compare the H_2O/CO ratio of the quasar with other $z \sim 6$ quasars that are detected in water emission. J0439+1634 was detected in the $H_2O(3_{2,1}–3_{1,2})$ emission and suggests a $L_{H_2O(3_{2,1}-3_{1,2})}/L_{CO(6-5)}$ ratio of 1.23 ± 0.22. Adopting a mean $H_2O(3_{2,1}–3_{1,2})/H_2O(2_{0,2}–1_{1,1})$ of 1.4 estimated from SMGs in

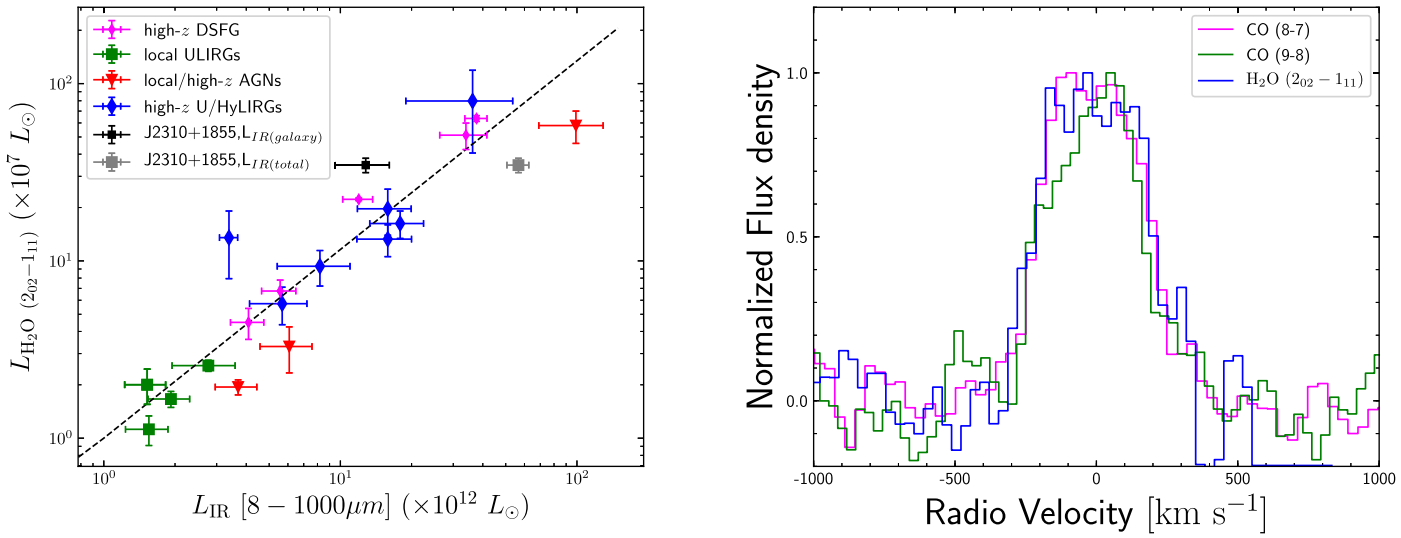

Figure 7. Left panel: $L_{H_2O(2_{0,2}-1_{1,1})}$ vs. L_{IR} (from Figure 3 in Yang et al. 2016). The green squares are the local ULIRGs from Yang et al. (2013), the blue diamonds are the high-redshift U/HyLIRGs from Yang et al. (2016), Omont et al. (2013), and van der Werf et al. (2011), the magenta diamonds are the high-redshift (dusty) star-forming galaxies from Jarugula et al. (2019) and Apostolovski et al. (2019), and the red down-triangles represent local and high-redshift AGNs, namely Mrk 231 (González-Alfonso et al. 2010), SDP81 (Yang et al. 2016), and APM 08279+5255 (Bradford et al. 2011) from left to right. Note that all of the luminosities plotted are intrinsic luminosities that have been corrected for lensing. The gray and black squares mark two cases of J2310+1855: the former (gray square) is the water line to total infrared luminosity ratio with $L_{IR(total)} = (5.7 \pm 0.6) \times 10^{13}\ L_\odot$ (with contributions from both quasar and host galaxy), and the latter (black square) shows the water line to galaxy infrared luminosity ratio with $L_{IR(galaxy)} = (1.4 \pm 0.3) \times 10^{13}\ L_\odot$ (which is purely from the host galaxy). The black dashed line represents the best fit to the local and high z U/HyLIRGs (green squares and blue diamonds) with $L_{H_2O(2_{0,2}-1_{1,1})} \sim L_{IR}^{1.06}$, see (Yang et al. 2016). Note that the definition of infrared luminosity is 8–1000 μm. Right panel: spectrum of CO(8–7) (magenta), (9–8) (green), and $H_2O(2_{0,2}-1_{1,1})$ (blue) normalized to the peak flux densities.

Yang et al. (2016), we estimate the $L_{H_2O}/L_{CO\ (6-5)}$ ratio in J0439+1634 of 0.86 ± 0.17, which is comparable to the value of J2310+1855.

We tentatively detected the OH^+ line at an S/N of 4. The spectra of the OH^+ line shows a P Cygni-like profile, with a possible absorption in the line center frequency. This might hint at possible outflows/inflows in this source, although further high-sensitivity observations are needed to confirm this. The ratios between OH^+, H_2O^+, and H_3O^+ reactive molecular ions are ideal tracers of the ionization rate and serve as the ionization source diagnostics. In J2310+1855, we are not able to constrain the ionization rate with the OH^+ detection alone. On the other hand, OH^+ and H_2O are all oxygen-hydrogen species, and OH^+ can be formed by photodissociation of H_2O. Accordingly, we are expecting a higher L_{OH^+}/L_{H_2O} ratio in the presence of cosmic-rays or X-rays. Mrk 231 is one of the best-studied AGNs that has been detected in a series of OH^+, H_2O^+, and H_3O^+ emission lines. González-Alfonso et al. (2018) detected very bright OH^+ emission with L_{OH^+}/L_{H_2O} ratio of 0.37 ± 0.13. The ionization rate derived by making use of all of the molecular ions detected is very high, and cannot even be explained by its observed X-ray flux and requires ionization by cosmic-rays (i.e., the ionization rate produced by X-ray photons is ∼1/10 the value required). The quasar J2310+1855 exhibits an L_{OH^+}/L_{H_2O} ratio of 0.20 ± 0.15, comparable with that of Mrk 231. The observed X-ray luminosity in J2310+1855 is ∼170× that observed in Mrk 231 (Vito et al. 2019). If we simply assume a similar ionization rate in J2310+1855 as that of Mrk 231 (as the L_{OH^+}/L_{H_2O} ratios are comparable in these two AGNs), the X-ray photons from J2310+1855 are more than adequate to explain the observed OH^+ emission.

5.5. Molecular Gas Heating Mechanisms

In the CO SLED modeling of J2310+1855, we find the mid to high J ($J \geqslant 5$) CO emission lines are dominated by a "warm" and "dense" gas component with $T \gtrsim 150$ K, $\log(n(H_2)/cm^{-3}) \gtrsim 5$, and $\log(N(CO)/cm^{-2}) \gtrsim 15.0$. Such "warm" and "dense" gas components are warmer and denser than typical values found in local (U)LIRGs (Papadopoulos et al. 2012, 2013), and comparable to the extreme cases, e.g., the NGC 1068 circumnuclear disk (Krips et al. 2011; Viti et al. 2014) and highly excited (U)LIRGs (Papadopoulos et al. 2012, 2013). Studies of local and high-redshift systems suggest that the molecular gas can be heated through (1) the UV heating from young massive stars or AGNs, (2) mechanical heating by shocks generated from supernovae or AGN outflows, (3) cosmic-ray heating from supernovae or AGNs, or (4) X-ray heating from the AGNs (Bradford et al. 2003, 2011; Spinoglio et al. 2012; Meijerink et al. 2013; Rosenberg et al. 2015; Uzgil et al. 2016). We inspect the most probable mechanism that contributes to the high CO excitation and luminous H_2O and OH^+ emission lines observed in J2310+1855.

To investigate the PDR origin, we fit the CO SLED of J2310+1855 to the PDR grid (Meijerink et al. 2007), and the best-fitting result indicates an FUV flux of $G_0 = 1.0 \times 10^4$ and $n \sim 5.6 \times 10^5\ cm^{-3}$. This suggests a higher FUV flux than that reported in Carniani et al. (2019) due to the lack of information from the $J \geqslant 10$ CO lines in their study. Although the CO emission can be explained by a dense PDR illuminated by an intense FUV radiation field, the bright H_2O and OH^+ emission lines (high H_2O/CO and OH^+/H_2O ratio) hint at different physical and chemical conditions than in a PDR, suggesting rather the presence of X-rays, shocks, or cosmic-rays that heat and ionize the molecular gas. In the nuclear region, both the star formation activity and the luminous quasar are capable of influencing the physical and chemical conditions of the molecular gas. The powerful quasar is able to participate in all of the possible gas heating mechanisms through the

X-rays it radiates, the shocks generated by AGN outflows, and the cosmic-rays it produces.

6. Summary

We report new detections of CO(5–4), (6–5), (12–11) and (13–12) with NOEMA and CO(8–7), (9–8), H_2O and OH^+ with ALMA in the $z = 6.003$ quasar J2310+1855. This is the most complete CO SLED ever obtained for a $z \geqslant 6$ quasar. We spatially resolved the CO(8–7), (9–8) and H_2O lines at similar source sizes of $\sim$2 kpc in FWHM, which are slightly more compact than the [C II] 158 μm and CO(2–1) emission lines. These suggest that the high J CO lines and the H_2O line are probing the nuclear dense molecular regions closer to the quasar. We analyze the physical conditions of the molecular gas through CO SLED modeling, and we also compare the CO emission lines from the quasar with local and high-redshift starburst samples and some representative local and high-redshift AGNs. The main results are summarized below.

1. The CO SLED of J2310+1855 at $J \geqslant 5$ is dominated by a "warm" and "dense" gas component in the parameter range of $T_{\rm kin} \approx 167^{+153}_{-56}$ K, $\log(n(\rm H_2)/\rm cm^{-3}) \approx 5.11^{+1.83}_{-0.58}$, and $\log(N(\rm CO)/\rm cm^{-2}) \approx 17.28^{+0.33}_{-0.42}$ (in the one-component model) or $T_{\rm kin} \approx 306^{+263}_{-149}$ K, $\log(n(\rm H_2)/\rm cm^{-3}) \approx 5.22^{+1.04}_{-0.49}$, and $\log(N(\rm CO)/\rm cm^{-2}) \approx 15.29^{+1.34}_{-1.17}$ (in the two-component model). We are not able to rule out a "cold" component that dominates the molecular gas mass but barely contributes to the $J \geqslant 5$ CO fluxes.
2. The CO SLED of J2310+1855 shows higher excitation compared to local/high-redshift starburst samples and local AGNs. Such high CO excitation is also found in other $z \gtrsim 6$ quasars (e.g., J1148+5251, J0100+2802, J0439+1634), and lensed high-redshift quasars (e.g., APM 08279+5255, the Cloverleaf).
3. The $L_{\rm H_2O}/L_{\rm IR(galaxy)}$ ratio in this quasar is higher than local and high z (U/Hy)LIRGs. The luminous detections of H_2O and OH^+ (high H_2O/CO and OH^+/H_2O ratios) are suggesting other heating and ionization sources (e.g., cosmic-rays, shocks, and X-rays) in addition to PDR. In the nuclear region, the luminous quasar and the starburst activity are able to impact on the molecular gas through all of these possible mechanisms.

Complete measurements of the CO SLED of the quasar hosts at $z \geqslant 6$ are of great importance for our understanding of the physical conditions and the heating mechanisms of the molecular gas in a complex environment with both AGN and nuclear starburst activity. It is also essential for higher-resolution observations to map the distributions and kinematics of the highly excited molecular gas around the AGN.

This work was supported by the National Science Foundation of China (11721303, 11991052) and the National Key R&D program of China (2016YFA0400702). We acknowledge Andres Asensio Ramos for his substantial help on the code MOLPOP-CEP. We thank Chentao Yang, Roberto Decarli, Toshiki Saito, and Daizhong Liu for important discussions. R.W. acknowledges support from the Thousand Youth Talents Program of China, and NSFC grants No. 11533001, and 11473004. D.R. acknowledges support from the National Science Foundation under grant numbers AST-1614213 and AST-1910107 and from the Alexander von Humboldt Foundation through a Humboldt Research Fellowship for Experienced Researchers. Y.G.'s research is supported by the National Key Basic Research and Development Program of China (grant No. 2017YFA0402704), the National Natural Science Foundation of China (grants No. 11861131007 and 11420101002), and the Chinese Academy of Sciences Key Research Program of Frontier Sciences (grant No. QYZDJSSW-SLH008). F.B. acknowledges support through the DFG Collaborative Research Centre 956. This paper is based on ALMA observations: ADS/JAO.ALMA 2015.1.01265.S. ALMA is a partnership of ESO (representing its member states), NSF (USA), and NINS (Japan), together with NRC (Canada), *MOST* and ASIAA (Taiwan), and KASI (Republic of Korea), in cooperation with the Republic of Chile. The Joint ALMA Observatory is operated by ESO, AUI/NRAO, and NAOJ. This paper also makes use of observations of IRAM NOEMA Interferometer: Project number W18EE. IRAM is supported by INSU/CNRS (France), MPG (Germany), and IGN (Spain).

ORCID iDs

Jianan Li https://orcid.org/0000-0002-1815-4839
Ran Wang https://orcid.org/0000-0003-4956-5742
Dominik Riechers https://orcid.org/0000-0001-9585-1462
Fabian Walter https://orcid.org/0000-0003-4793-7880
Roberto Decarli https://orcid.org/0000-0002-2662-8803
Roberto Neri https://orcid.org/0000-0002-7176-4046
Yali Shao https://orcid.org/0000-0002-1478-2598
Xiaohui Fan https://orcid.org/0000-0003-3310-0131
Chris L. Carilli https://orcid.org/0000-0001-6647-3861
Alain Omont https://orcid.org/0000-0002-4721-3922
Karl M. Menten https://orcid.org/0000-0001-6459-0669
Frank Bertoldi https://orcid.org/0000-0002-1707-1775
Desika Narayanan https://orcid.org/0000-0002-7064-4309

References

Apostolovski, Y., Aravena, M., Anguita, T., et al. 2019, A&A, 628, A23
Asensio Ramos, A., & Elitzur, M. 2018, A&A, 616, A131
Bañados, E., Decarli, R., Walter, F., et al. 2015, ApJL, 805, L8
Beelen, A., Cox, P., Benford, D. J., et al. 2006, ApJ, 642, 694
Bertoldi, F., Carilli, C. L., Cox, P., et al. 2003, A&A, 406, L55
Bertoldi, F., Cox, P., Neri, R., et al. 2003, A&A, 409, L47
Blake, G. A., Sutton, E. C., Masson, C. R., & Phillips, T. G. 1987, ApJ, 315, 621
Bothwell, M. S., Aguirre, J. E., Aravena, M., et al. 2017, MNRAS, 466, 2825
Bothwell, M. S., Smail, I., Chapman, S. C., et al. 2013, MNRAS, 429, 3047
Bradford, C. M., Aguirre, J. E., Aikin, R., et al. 2009, ApJ, 705, 112
Bradford, C. M., Bolatto, A. D., Maloney, P. R., et al. 2011, ApJL, 741, L37
Bradford, C. M., Nikola, T., Stacey, G. J., et al. 2003, ApJ, 586, 891
Carilli, C. L., & Walter, F. 2013, ARA&A, 51, 105
Carniani, S., Gallerani, S., Vallini, L., et al. 2019, MNRAS, 489, 3939
Da Cunha, E., Groves, B., Walter, F., et al. 2013, ApJ, 766, 13
Daddi, E., Dannerbauer, H., Liu, D., et al. 2015, A&A, 577, A46
Decarli, R., Walter, F., Venemans, B. P., et al. 2018, ApJ, 854, 97
Elitzur, M., & Asensio Ramos, A. 2006, MNRAS, 365, 779
Falgarone, E., Zwaan, M. A., Godard, B., et al. 2017, Natur, 548, 430
Feruglio, C., Fiore, F., Carniani, S., et al. 2018, A&A, 619, A39
Fixsen, D. J., Bennett, C. L., & Mather, J. C. 1999, ApJ, 526, 207
Foreman-Mackey, D., Hogg, D. W., Lang, D., & Goodman, J. 2013, PASP, 125, 306
Gallerani, S., Ferrara, A., Neri, R., & Maiolino, R. 2014, MNRAS, 445, 2848
González-Alfonso, E., Fischer, J., Aalto, S., & Falstad, N. 2014, A&A, 567, A91
González-Alfonso, E., Fischer, J., Bruderer, S., et al. 2018, ApJ, 857, 66
González-Alfonso, E., Fischer, J., Isaak, K., et al. 2010, A&A, 518, L43
Goodman, J., & Weare, J. 2010, Communications in Applied Mathematics and Computational Science, 5, 65
Greve, T. R., Leonidaki, I., Xilouris, E. M., et al. 2014, ApJ, 794, 142

Guilloteau, S., & Lucas, R. 2000, in ASP Conf. Ser. 217, Imaging at Radio through Submillimeter Wavelengths 217, ed. J. G. Mangum & S. E. J. Radford (San Francisco, CA: ASP), 299
Habart, E., Dartois, E., Abergel, A., et al. 2010, A&A, 518, L116
Hashimoto, T., Inoue, A. K., Tamura, Y., et al. 2018, arXiv:1811.00030
Jarugula, S., Vieira, J. D., Spilker, J. S., et al. 2019, ApJ, 880, 92
Jiang, L., Fan, X., Vestergaard, M., et al. 2007, AJ, 134, 1150
Jiang, L., McGreer, I. D., Fan, X., et al. 2016, ApJ, 833, 222
Jin, S., Daddi, E., Magdis, G. E., et al. 2019, ApJ, 887, 144
Kamenetzky, J., Glenn, J., Rangwala, N., et al. 2012, ApJ, 753, 70
Kollatschny, W., Weilbacher, P. M., Ochmann, M. W., et al. 2019, arXiv:1910.12813
Kormendy, J. 1993, in IAU Symp. 153, Galactic Bulges, ed. H. DeJonghe & H. Jan Habing (Dordrecht: Kluwer), 209
Kormendy, J., & Ho, L. C. 2013, ARA&A, 51, 511
Krips, M., Martín, S., Eckart, A., et al. 2011, ApJ, 736, 37
Leipski, C., Meisenheimer, K., Walter, F., et al. 2013, ApJ, 772, 103
Liu, D., Gao, Y., Isaak, K., et al. 2015, ApJL, 810, L14
Maiolino, R., Cox, P., Caselli, P., et al. 2005, A&A, 440, L51
Maiolino, R., Gallerani, S., Neri, R., et al. 2012, MNRAS, 425, L66
McMullin, J. P., Waters, B., Schiebel, D., Young, W., & Golap, K. 2007, adass XVI, 376, 127
Meijerink, R., Kristensen, L. E., Weiß, A., et al. 2013, ApJL, 762, L16
Meijerink, R., & Spaans, M. 2005, A&A, 436, 397
Meijerink, R., Spaans, M., & Israel, F. P. 2007, A&A, 461, 793
Meijerink, R., Spaans, M., Loenen, A. F., et al. 2011, A&A, 525, A119
Neeleman, M., Banados, E., Walter, F., et al. 2019, ApJ, 882, 10
Novak, M., Bañados, E., Decarli, R., et al. 2019, ApJ, 881, 63
Odorico, D'., Feruglio, V., & Ferrara, C. 2018, ApJL, 863, L29
Omont, A., Yang, C., Cox, P., et al. 2013, A&A, 551, A115
Panuzzo, P., Rangwala, N., Rykala, A., et al. 2010, A&A, 518, L37
Papadopoulos, P. P., van der Werf, P. P., Xilouris, E. M., et al. 2012, MNRAS, 426, 2601
Papadopoulos, P. P., Zhang, Z.-Y., Weiss, A., et al. 2013, in IAU Symp. 292, Molecular Gas, Dust, and Star Formation in Galaxies (Cambridge: Cambridge Univ. Press), 209
Pellegrini, E. W., Smith, J. D., Wolfire, M. G., et al. 2013, ApJL, 779, L19
Putaud, T., Michaut, X., Le Petit, F., et al. 2019, A&A, 632, A8
Riechers, D. A., Bradford, C. M., Clements, D. L., et al. 2013, Natur, 496, 329
Riechers, D. A., Carilli, C. L., Maddalena, R. J., et al. 2011, ApJL, 739, L32
Riechers, D. A., Leung, T. K. D., Ivison, R. J., et al. 2017, ApJ, 850, 1
Riechers, D. A., Walter, F., Carilli, C. L., et al. 2006, ApJ, 650, 604
Riechers, D. A., Walter, F., Carilli, C. L., & Lewis, G. F. 2009, ApJ, 690, 463
Rosenberg, M. J. F., van der Werf, P. P., Aalto, S., et al. 2015, ApJ, 801, 72
Shao, Y., Wang, R., Carilli, C. L., et al. 2019, ApJ, 876, 99
Shao, Y., Wang, R., Jones, G. C., et al. 2017, ApJ, 845, 138
Spinoglio, L., Pereira-Santaella, M., Busquet, G., et al. 2012, ApJ, 758, 108
Stanley, F., Jolly, J. B., König, S., et al. 2019, A&A, 631, A78
Uzgil, B. D., Bradford, C. M., Hailey-Dunsheath, S., Maloney, P. R., & Aguirre, J. E. 2016, ApJ, 832, 209
van der Werf, P. P., Berciano Alba, A., Spaans, M., et al. 2011, ApJL, 741, L38
van der Werf, P. P., Isaak, K. G., Meijerink, R., et al. 2010, A&A, 518, L42
Venemans, B. P., Neeleman, M., Walter, F., et al. 2019, ApJL, 874, L30
Venemans, B. P., Walter, F., Decarli, R., et al. 2017a, ApJ, 845, 154
Venemans, B. P., Walter, F., Decarli, R., et al. 2017b, ApJL, 851, L8
Viti, S., García-Burillo, S., Fuente, A., et al. 2014, A&A, 570, A28
Vito, F., Brandt, W. N., Bauer, F. E., et al. 2019, A&A, 630, A118
Volonteri, M. 2012, Sci, 337, 544
Walter, F., Bertoldi, F., Carilli, C., et al. 2003, Natur, 424, 406
Walter, F., Carilli, C., Bertoldi, F., et al. 2004, ApJL, 615, L17
Walter, F., Riechers, D., Cox, P., et al. 2009, Natur, 457, 699
Walter, F., Riechers, D., Novak, M., et al. 2018, ApJL, 869, L22
Walter, F., Riechers, D. A., Carilli, C. L., et al. 2007, in ASP Conf. Ser. 375, From Z-Machines to ALMA: (Sub)Millimeter Spectroscopy of Galaxies, ed. A. J. Baker et al. (San Francisco, CA: ASP), 182
Wang, F., Wang, R., Fan, X., et al. 2019a, ApJ, 880, 2
Wang, R., Carilli, C. L., Neri, R., et al. 2010, ApJ, 714, 699
Wang, R., Carilli, C. L., Wagg, J., et al. 2008, ApJ, 687, 848
Wang, R., Shao, Y., Carilli, C. L., et al. 2019b, ApJ, 887, 40
Wang, R., Wagg, J., Carilli, C. L., et al. 2011a, AJ, 142, 101
Wang, R., Wagg, J., Carilli, C. L., et al. 2011b, ApJL, 739, L34
Wang, R., Wagg, J., Carilli, C. L., et al. 2013, ApJ, 773, 44
Wang, R., Wu, X.-B., Neri, R., et al. 2016, ApJ, 830, 53
Weiß, A., Downes, D., Neri, R., et al. 2007, A&A, 467, 955
Weiß, A., Requena-Torres, M. A., Güsten, R., et al. 2010, A&A, 521, L1
Weiß, A., Walter, F., & Scoville, N. Z. 2005, A&A, 438, 533
Yang, C., Gao, Y., Omont, A., et al. 2013, ApJL, 771, L24
Yang, C., Omont, A., Beelen, A., et al. 2016, A&A, 595, A80
Yang, C., Omont, A., Beelen, A., et al. 2017, A&A, 608, A144
Yang, J., Venemans, B., Wang, F., et al. 2019, ApJ, 880, 153
Zhang, Z.-Y., Papadopoulos, P. P., Ivison, R. J., et al. 2016, RSOS, 3, 160025